Large-Scale Filaments From Weak Lensing

by

Seth Epps

A thesis
presented to the University of Waterloo
in fulfillment of the
thesis requirement for the degree of
Master of Science
in
Physics

Waterloo, Ontario, Canada, 2015

I hereby declare that I am the sole author of this thesis. This is a true copy of the thesis, including any required final revisions, as accepted by my examiners.

I understand that my thesis may be made electronically available to the public.

Abstract

In the context of non-linear structure formation, a web of dark filaments are expected to intersect the high density regions of the universe, where groups and clusters of galaxies will be forming. In this work we have developed a method for stacking the weak lensing signal of an ensemble of filaments between groups and clusters of galaxies. We detect a the weak lensing signal from stacked filaments between SDSS BOSS luminous red galaxies with the CFHTLenS data at the 5σ level, finding a mass of $(1.6 \pm 0.3) \times 10^{13} M_{\odot}$. Two methods of isolating the filament signal are presented: the method of non-physical pair subtraction, and the method of outside region subtraction. This signal is compared with the three-point galaxy-galaxy-convergence correlation function, as developed in Clampitt et al. (2014), yielding reasonably good agreement.

Acknowledgements

I would like to thank my adviser Mike Hudson for his guidance, patience, and contributions.

Table of Contents

List of Figures

Chapter 1

Introduction

For the past half century there has been immense progress in the field of cosmology, with the development of new observational equipment and the increased power of numerical simulations physicists have advanced our understanding of the structures in our universe and their origin. The formation of these structures is thought to be governed by dark matter, which makes up more than 80% of all matter in our universe, and stems from the growth of fluctuations in the primordial universe.

In the past few decades there has been substantial observational evidence supporting that our universe is described by a ΛCDM cosmological model (*e.g.*, see Planck Collaboration et al., 2015). In this universe the dominant component of energy density is dark energy, the second largest being dark matter, and only a tiny fraction comprised of the baryonic matter. The evidence for dark matter is extensive, and has dated back nearly 100 years with Fritz Zwicky noting the radial velocities of galaxies in the Coma cluster exceeded the amount that the baryonic matter could support gravitationally. He concluded that there must exist what he referred to as "dunkle Materie" Zwicky (1933) or "dark matter".

As the field has progressed, theory and simulations have predicted that galaxies, and clusters of galaxies organize themselves into dark matter halos, but these only make up a fraction of the "cosmic web", consisting of voids, sheets, and filaments of dark matter. In particular, the halos that clusters of galaxies live in make up the nodes of the cosmic web, at the intersection of filaments. Unfortunately, the evidence for the extended dark matter structures that make up the cosmic web is significantly lacking, especially on a global scale across the universe, with only a few individual filament detections. As a result, mapping out the large scale structure of the universe is one of the biggest challenges in modern

cosmology.

Traditionally dark matter is inferred from dynamical methods, similar to the way Zwicky did in the early 20th century. Recently, the development of weak gravitational lensing has provided an extremely powerful alternative method to map out dark matter. Dark matter acts as a lens for the light passing from distant galaxy, distorting their shapes, giving a direct probe of the underlying distribution of dark matter.

In this chapter we introduce structure formation from the standpoint of linear perturbation theory and extend this into the formation of non-linear structures. Weak gravitational lensing is outlined as a tool for measuring the distribution of dark matter, and its application in galaxy-galaxy lensing studies. At the end of this chapter we summarize the current observational evidence for dark matter filaments, and give the outline of this thesis.

1.1 Structure Formation

1.1.1 Linear Structure Formation

Often when the universe is being described, it is done under the assumption of that the universe is both homogenous and isotropic. In fact, this is a reasonable description on the largest scales of the universe, however we know this can't be completely true because we observe structures on smaller scales, going from solar systems all the way to clusters of galaxies. The standard process by which these structures are formed is through the growth of primordial fluctuations through gravitational instability.

In this scenario, the universe was initially in some nearly homogenous state save some tiny fluctuations relative to the background density, as confirmed by observations of the Cosmic Microwave Background (CMB). The exact origin of these fluctuations is not well understood. The general consensus is that quantum fluctuations were imprinted on universe through a rapid period of inflation. As long as these fluctuations are small enough, they can be treated as linear perturbations to the background density and worked out completely.

The key quantity of interest in linear perturbation theory is the fractional difference in

density relative to the background universe density, or "density contrast",

$$\delta(\vec{x}) = \frac{\rho(\vec{x}) - \overline{\rho}}{\overline{\rho}}. \tag{1.1}$$

Linear perturbation theory applies in the limit that $|\delta| \ll 1$, *i.e.*, when the contrast/fluctuations are very small. The density contrast can be combined with conservation of energy, Euler's equation, and the Poisson equation to get the time evolution of the density contrast, containing all of the information about density fluctuations in the early universe,

$$\ddot{\delta} + 2\frac{\dot{a}}{a}\dot{\delta} - 4\pi G\overline{\rho}\delta = 0. \tag{1.2}$$

There are two solutions to (1.2): one growing mode (D_1), and the other decaying (D_2). Since we are concerned with the *growth* of fluctuations it is only necessary to focus on the growing mode solution. Furthermore, since (1.2) is only differential in time, the solutions can be separated into a spatial component and a temporal component, with general solution

$$\delta(\vec{x}, t) = D_1(t)\delta_1(\vec{x}) + D_2(t)\delta_2(\vec{x}). \tag{1.3}$$

Equation (1.3) applies to a single Fourier mode of the density fluctuations, so it is often more convenient to work in Fourier space to specify the properties of fluctuations,

$$\tilde{\delta}(\vec{k}, t) \propto \int d^3\vec{x}\delta(\vec{x}, t)e^{i(\vec{k}\cdot\vec{x})}, \tag{1.4}$$

where the statistics of all fluctuation modes are described by the power spectrum of fluctuations, $P(k) \equiv \left\langle |\tilde{\delta}(\vec{k})|^2 \right\rangle$. As it turns out, a simple inflationary model predicts that the primordial power spectrum follows a power-law, $P(k) \propto k^{n_s}$, with $n_s \simeq 1$, and the fluctuations are characterized by a gaussian random field. This implies that,

$$\left\langle \tilde{\delta}(\vec{k}1)\tilde{\delta}(\vec{k}_2) \right\rangle = P(k_1)\delta_{\mathrm{D}}(k_1 - k_2), \tag{1.5}$$

where δ_{D} is the Dirac delta function, which ensures that the k-modes evolve independent of each other. The magnitude only dependance of $P(k)$ comes from isotropy and homogeneity of the universe.

In order to complete the picture, the power spectrum needs to capture the evolution of modes outside the horizon as they enter, all the way to the epoch of decoupling. This is encoded in the transfer function $T(k)$ giving the complete power spectrum,

$$P_{\mathrm{m}}^{\mathrm{L}}(k, t) \propto k^{n_s}T^2(k)D^2(t). \tag{1.6}$$

3

The power spectrum in (1.6) describes the general shape, however to completely specify the power spectrum one needs information about the overall amplitude. With the initial conditions of the universe being unknown, the constant of proportionality cannot be fixed a priori, but through observations.

The analogous configuration space counter-part to the power spectrum is the two-point correlation function; the Fourier transform of the power spectrum,

$$\xi(\vec{r}) \equiv \langle \delta(\vec{x} + \vec{r})\delta(\vec{x}) \rangle = \int \frac{d^3\vec{k}}{(2\pi)^3} P(k) e^{i(\vec{k}\cdot\vec{r})}. \tag{1.7}$$

The physical interpretation of the correlation function is as the probability that two particles (*e.g.*, galaxies) can be found separated by $|\vec{r} - \vec{x}|$, beyond random probability. This is often the tool used to probe galaxy clustering; if objects are clustered ($\xi > 0$) there is a probability enhancement over a random distribution.

1.1.2 Non-Linear Structure Formation

As the fluctuations grow out of the linear regime ($\delta(\vec{x}) \gtrsim 1$), the formalism above is no longer sufficient to describe the growth of structure in the universe, and they enter the *non-linear* regime. The simplest (yet extremely useful) model for the growth of fluctuations in the non-linear regime is the spherical top-hat model, which describes the gravitational collapse of a uniform overdense sphere. The standard assumption in this model is that the density contrast within some radius is constant, $\delta(< R) = \bar{\delta}$, and outside it is simply 0, $\delta(> R) = 0$.

It turns out, as a result of Birkhoff's theorem, in this simplified model the physical radius of the overdensity obeys the exact same equations as the cosmological scale factor for a positively curved matter dominated "sub"-universe embedded a background universe with a lower mean density. Using the same parametric solution as the positive curved universe the resulting behaviour of the overdense region is (Padmanabhan, 1993)

$$
\begin{aligned}
R(\theta) &= \frac{R_{\mathrm{m}}}{2}\left(1 - \cos(\theta)\right) \\
t(\theta) &= \frac{R_{\mathrm{m}}}{2c}\left(\theta - \sin(\theta)\right),
\end{aligned}
\tag{1.8}
$$

where R_{m} is the maximum radius of the spherical overdensity. In this parameterization, the sphere will reach a maximum radius when $\theta = \pi$, and will be "collapsed" when $\theta = 2\pi$.

The usefulness of this approximation isn't immediately obvious. When the equations are expanded for small times, a correctly scaled result of the linear perturbation density contrast for a matter dominated universe is recovered, as it should. If we map the time of collapse as calculated from the spherical top-hat back to the linear theory, we get that $\delta_{\text{lin}} \sim 1.69$. This simple model allows us to follow the density contrast as with linear perturbations, and once the contrast has reached $\delta_{\text{lin}} \gtrsim 1$ we expect the region to have collapsed with a substantial density contrast according to a non-linear prescription.

Of course, this isn't the way structures form in the universe, but a very limited approximation. A different way to think of structure formation is through a hierarchy in which smaller structures collapse first, overcoming the expansion on the universe and subsequently larger and larger structures form. This is commonly referred to as "Hierarchical Structure Formation", and is a prediction of a typical cold dark matter (CDM) model. In this picture, it is expected that small "halos" will form from the enhanced density perturbations laid out at inflation, and then through mergers these halos will attract and merge, forming larger halos.

Beyond spherical (or a slightly more generalized ellipsoidal) collapse model, there is very little analytic treatment of non-linear structure. An early theoretical treatment of the formation of non-linear structure is from work done by Zel'dovich (1970), where primordial fluctuations evolve into the non-linear regime by the *Zel'dovich approximation*. This captured a lot of the qualitative features of the large scale structure, displaying a weblike pattern. The approximation had certain short-comings, such as the lack of formation of high density collapsed regions. Naturally, to investigate the behaviour of matter in the non-linear regime one turns to cosmological simulations, the simplest[1] of which are pure dark matter "N-Body" simulations. In N-body simulations, the dark matter is treated as a collisionless fluid with no hydrodynamic properties and subsequently discretized into tracer particles, which represent a collection of particles.

One approach to the N-body problem is to just solve the gravitational potential at all locations,

$$\Phi(\vec{r}) = -G \sum_j \frac{m_j}{(|\vec{r} - \vec{r_j}|^2 + \epsilon^2)^{3/2}} \tag{1.9}$$

where the sum is over all j tracer particles. Φ is *almost* exactly the Newtonian potential, from which the set particles acceleration can be generated. A softening length, ϵ, is introduced to reduce the effect of spurious two-body interactions. This is the most accurate technique for simulations involving dark matter only, but there is a computational trade-off

---

[1]Simple is a relative term here, referring to the fewest "ingredients" needed.

as it is very CPU-intensive. There are optimizations that can be made to speed up the simulation, *e.g.*, Tree or Fourier methods, like Particle-Mesh methods (Dolag et al., 2008).

The results from N-body simulations are rather spectacular, capturing the evolution of primordial fluctuations all the way to the high density collapsed regions (see Figure 1.1), resembling the distribution galaxies in redshift surveys. One of the most notable features of the distribution of dark matter in N-body simulations is the filamentary structures that form, intersecting the high density nodes. These filaments are the structures of particular interest. Following the evolution of the particles also confirms the notion of a bottom-up hierarchy where an initial overdensity first collapse into a sheet, then along a filaments, and finally into a halo (*e.g.*, Cautun et al., 2014).

The characterization of filaments in N-body simulations is complicated. Anisotropic collapse of structures in N-body simulations has been done using tidal forces, with filaments naturally forming between primordial overdensities (Bond et al., 1996; Weygaert and Bond, 2008). This picture gives rise to the formation of filaments between groups and clusters of galaxies. In this work we assume that filaments will form between groups and clusters of galaxies. More recently, Colberg et al. (2005) attempted to classify filaments that intersect cluster pairs in N-body simulations by properties such as length, and likelihood of connections.

An alternative method for characterizing filaments is through higher order perturbations. To some degree non-linear structure can be treated using perturbation theory, however it requires expanding perturbation theory with higher order terms. As δ approaches unity, perturbations enters the weakly non-linear regime, and the fluctuation modes no longer evolve independently. In this regime the power spectrum (1.6) no longer completely describes the statistics of fluctuation. In the context of the power spectrum, the mixing of scales at lowest order can be characterized by the bispectrum, and can be worked out analytically in perturbation theory (Goroff et al., 1986; Jain and Bertschinger, 1994; Bernardeau et al., 2002).

The correlation function corresponding to the bispectrum, the three-point correlation, is one way to model the weakly non-linear filamentary structure that is seen in numerical simulations. From a probabilistic view the three-point correlation function represents the probability that there is a third point correlated with two other given points. That is to say, if there are two clusters at fixed locations, what is the probability that there is excess matter at any point around them, *beyond* the sum of the two-point correlation contribution from the two clusters (Peebles, 1980). In this work we attempt to measure this three-point
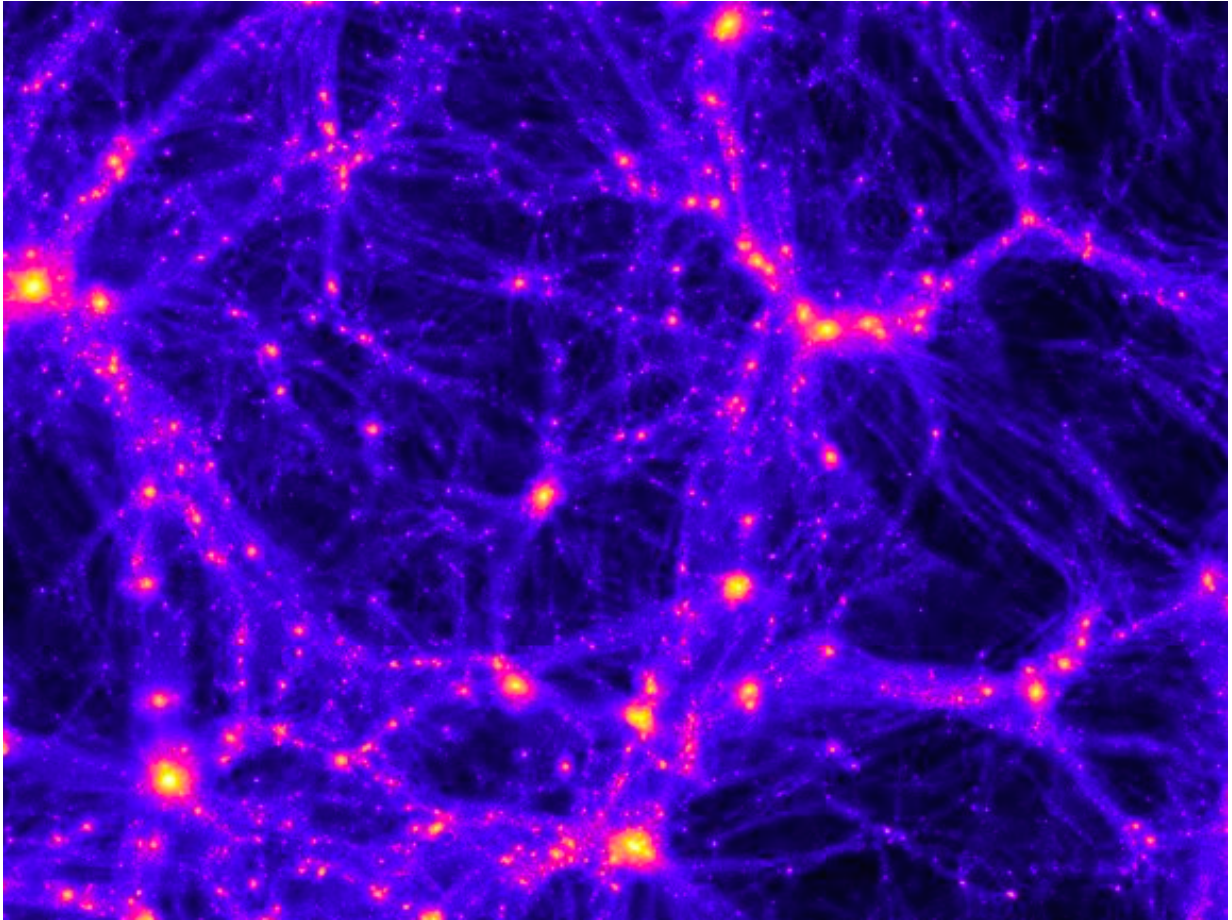
Figure 1.1: A snapshot of the dark matter distribution in the EAGLE Simulation (Schaye et al., 2015). This shows the formation of high density nodes (bright orange) woven into the relatively low density cosmic web.

correlation function through weak gravitational lensing.

1.2 Weak Gravitational Lensing

One of the predictions of General Relativity is that the presence of mass bends space-time and the path of photons travelling near this mass will be deflected, a phenomena known as gravitational lensing. The gravitational lensing of light from galaxies can be separated into two regimes: strong lensing where the light passing by some matter distribution is split into multiple rays, and weak lensing where the shape of the photon source is only distorted. Strong lensing is rather limited in its application because it requires the lensing matter to have a very high density and more specific source-lens-observer geometry. Weak lensing on the other hand is much more useful as a tool and can be applied to the majority of the universe.

In the typical weak gravitational lensing system, we consider source light that originates from a background galaxy (source) that under the gravitational influence of a foreground matter distribution (lens). In this lensing system any photon deflection is extremely small, and as such only a small cone along the line of sight needs to be considered. In this approximation, the lens and source lie in planes perpendicular to the line of sight (See Figure 1.2). The lens lies in a plane at redshift z_d (angular diameter distance D_d) and the source at redshift z_s (angular diameter distance D_s), relative to an observer, with the distance between the lens plane and source plane is an angular diameter distance D_ds.

Figure 1.2 shows general lensing scenario with a source at position $\vec{\eta}$ (in the source plane) and lens at position $\vec{\xi}$ (in the lens plane), with the deflection angle in the lens plane, $\vec{\hat{\alpha}}$. From the geometry in Figure 1.2, it can be shown that the true position of the source, $\vec{\beta}$, will be seen by an observer at $\vec{\theta}$, being shifted by the "scaled deflection", $\vec{\alpha}(\vec{\theta})$. The scaled deflection is related to the surface mass density by (Schneider, 2006)

$$\vec{\alpha} = \pi^{-1} \int d^2\vec{\theta'} \kappa(\vec{\theta'}) \frac{\vec{\theta} - \vec{\theta'}}{|\vec{\theta} - \vec{\theta'}|^2}, \tag{1.10}$$

where κ is defined as the dimensionless surface density or *convergence*,

$$\kappa(\vec{\theta}) \equiv \frac{\Sigma(D_\mathrm{d}\vec{\theta})}{\Sigma_\mathrm{crit}}. \tag{1.11}$$
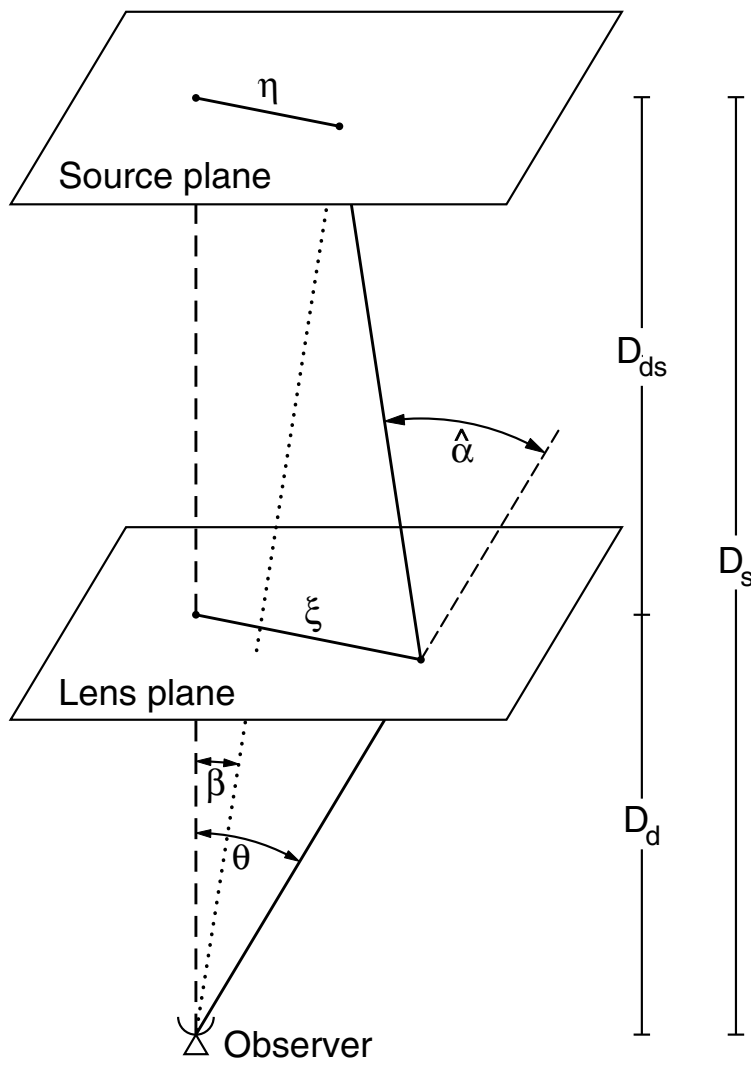
Figure 1.2: A diagram of the lens-source-observer geometry in a typical gravitational lensing scenario, illustrating the path a photon takes from source to observer – Reproduced from Schneider (2006)

Here Σ_{crit} is the critical surface mass density of the lens which depends on all distances between observer, lens, and source,

$$\Sigma_{\text{crit}} \equiv \frac{c^2}{(4\pi G)} \frac{D_{\text{s}}}{D_{\text{d}} D_{\text{ds}}}, \tag{1.12}$$

and Σ is the surface mass density of the lens projected along the line-of-sight. The convergence, or equivalently Σ_{crit}, can be used as a way to quantify the division of gravitational lensing into the weak and strong regimes. A lens with $\Sigma(\vec{\theta}) \gtrsim \Sigma_{\text{crit}}$ will produce multiple images for certain $\vec{\theta}$, and a lens with $\Sigma(\vec{\theta}) \ll \Sigma_{\text{crit}}$ will only produce *shearing* of the source image in the lens plane.

Without multiple images, one must have some knowledge of the sources in order to measure the effect of the lens on the source shear. In the weak lensing regime the sources are treated as ellipses, and the lens will coherently distort the shape of the source ellipse, stretching and shearing it, as mentioned above. This stretching and shearing of the sources is described by the reduced shear (Schneider, 2006),

$$g(\vec{\theta}) = \frac{\gamma(\vec{\theta})}{[1 - \kappa(\vec{\theta})]}, \tag{1.13}$$

where $\gamma(\vec{\theta})$ is the 'shear', and $\kappa(\vec{\theta})$ is the convergence defined above. In this formalism, the stretching of the source elliptical shape is described by γ and the magnification of the image by κ. In the weak lensing limit, $\kappa \ll 1$ and the reduced shear, g, just becomes the shear, γ, which is described by a two component polarization vector, $\gamma = (\gamma_1, \gamma_2)$ (see Figure 1.3). The ellipticity of the background source can then be related to the shear through,

$$e^{\text{I}} = e^{\text{S}} + \gamma, \tag{1.14}$$

where $e^{(\text{I,S})}$ is the two component ellipticity polarization vector describing the shape of the background source in the image (e^{I}), and the intrinsic source shape (e^{S}). If there is no preferred direction for the intrinsic shape an ensemble average of many sources gives,

$$\langle e^{\text{I}} \rangle = \langle \gamma \rangle . \tag{1.15}$$

The accuracy of the weak lensing signal depends the quality shape measurements for source galaxies. The two component polarization vector that describes the shape, e, can be measured from the quadrupole moments of the galaxy intensity distribution (Kaiser et al.,

1995),

$$
\begin{aligned}
e_1 &= \frac{Q_{11} - Q_{22}}{Q_{11} + Q_{22}} \\
e_2 &= \frac{2Q_{12}}{Q_{11} + Q_{22}},
\end{aligned}
\tag{1.16}
$$

where Q_{ij} are the weighted intensity quadrupoles of the galaxy image. With this method of shape measurement one must be cautious as there will be effects from point spread function anisotropies and smearing, introducing spurious signal. Fortunately, these effects can be corrected after making a shape measurement.

In order to estimate distances to galaxies in lensing experiments one needs galaxy redshifts. Spectroscopic redshifts that rely on spectral features provide the most accurate estimate of the source redshift. For large surveys spectroscopy becomes expensive and time consuming making it an impractical approach. A more 'cost-effective' approach is to use multi-band photometry to estimate a galaxy's redshift. The standard approach for estimating the redshift from photometry is fitting templates based on spectral energy distributions of galaxies of known redshift (Connolly et al., 1995).

The unfortunate downside to using photometry to estimate the redshift is the substantially larger errors, typically on the order of $\sigma_z \sim 0.04(1 + z)$, for example see Hildebrandt et al. (2012), as compared with spectroscopic redshifts which are ~ 2 orders of magnitude smaller. Additionally, they suffer from the possible 'catastrophic' failure where the redshift probability density appears bimodal. As a result, the error on photometric redshifts can increase by an order of magnitude. In CFHTLenS the catastrophic failure rate is less than 4% (Hildebrandt et al., 2012), and ultimately these errors do not constitute the dominant source of uncertainty in the lensing measurements.

1.2.1 Galaxy-Galaxy Lensing

Galaxy-galaxy lensing (GGL) is the application of weak lensing when both the lens and source are galaxies. The idea is that if galaxies house the amount of dark matter as suggested by dynamical methods, they should act as a weak lens for background source galaxies. For an individual galaxy, depending on the mass, this may not be an appreciable effect, but averaging over tens of thousands of galaxies with similar properties could probe the density of the host dark matter halos out to radii on the order of 1Mpc, much further than possible with other methods. With large enough galaxy samples, it is even possible
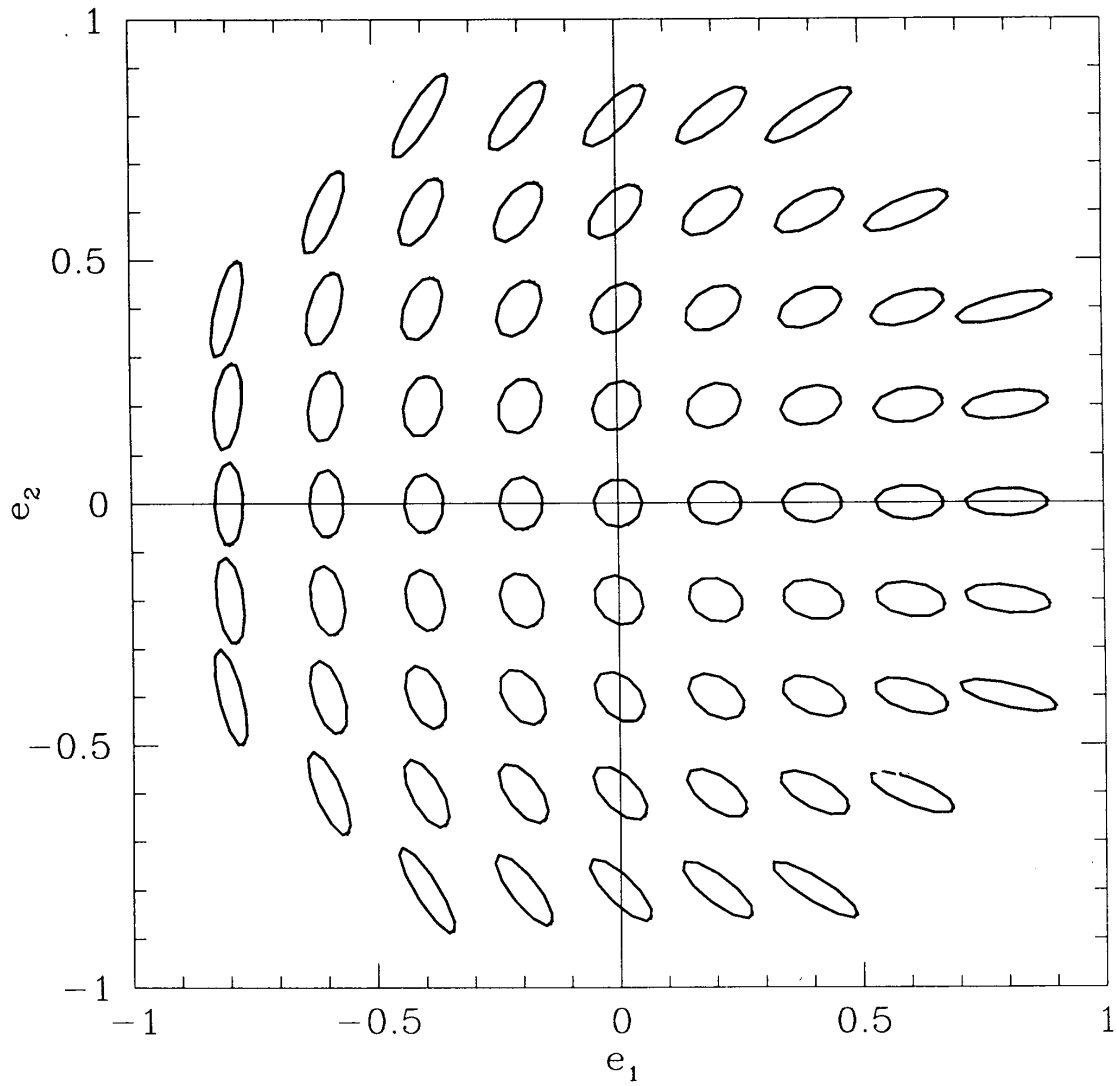
Figure 1.3: The ellipticity plane showing the galaxy shape components, e_1 and e_2. – Taken from Kaiser et al. (1995)

to separate the galaxies into different classes based on luminosity, redshift, or morphology. The disadvantage of stacking many galaxies as weak lenses is that the signal is an ensemble average over many similar lenses, so they can only be probed in a statistical context.

A feature of spherically symmetric matter distributions is that they, to first order, produce only tangential shearing of background sources. In other words the galaxy shape is stretched along an imaginary circle about the lens centre. One can also define the cross-shear, where the shearing is along the axis 45° to the tangent, similar to a 'curl' mode. This gives a useful systematic test as it should be 0 for a spherically symmetric lens. The tangential shear is directly proportial to the excess surface density of the lens, defined by (Schneider, 2006)

$$\Delta\Sigma(R) \equiv \overline{\Sigma(<R)} - \overline{\Sigma(R)} = \Sigma_{\mathrm{crit}} \left\langle \gamma_{\mathrm{T}}(R) \right\rangle, \tag{1.17}$$

where $\langle \gamma_{\mathrm{T}} \rangle$ is the ensemble average of source tangential shears at radius R, and Σ_{crit} is the critical surface density defined in (1.12). This gives a direct way to constrain properties of dark matter halos, such as the mass and shape of the host halo to galaxies and clusters of galaxies, or following the evolution of galaxies with their dark matter halos through cosmic time (Hudson et al., 2015).

1.2.2 Kaiser & Squires Reconstruction

A fundamental problem with analyzing shears in weak lensing is that they do not have any direct interpretation. In galaxy-galaxy lensing, the *tangential* shear has a very direct interpretation (see equation 1.17). In general, however, the lens won't necessarily have spherical symmetry (*e.g.*, filaments), it is much easier to examine the convergence or surface mass density. Kaiser and Squires (1993) introduced a method of reconstructing the convergence from the weak lensing shear field. They recognized that the shear vector is just a convolution of the convergence, κ, with some lensing kernel $D(\theta)$,

$$\gamma = \frac{1}{\pi} \int d^2\theta' D(\theta - \theta')\kappa(\theta'). \tag{1.18}$$

One can then "de-convolve" the shear field to get the convergence field,

$$\kappa(\theta) - \kappa_0 = \frac{1}{\pi} \int d^2\theta' D^*(\theta - \theta')\gamma(\theta'), \tag{1.19}$$

Where D^* is the complex conjugate of the kernel $D(\theta)$. This is in essence the method of reconstruction. *Given κ one can invert to get γ, and vice-versa.* The additive constant, κ_0,

in (1.19) is a manifestation of the mass sheet degeneracy, *i.e.*, if a sheet constant surface density is added across the entire field, the shear remains unchanged. To overcome the mass-sheet degeneracy, one needs more information than just the shears, for example the magnification (Schneider, 2006). It is relatively straightforward to solve (1.18) and (1.19) using the method of Fast Fourier Transforms.

1.3   Summary Of Current Observations

Weak lensing seems to be the optimal tool for detecting filaments in the large-scale structure of the universe as it doesn't require any prior knowledge of the filaments or any assumptions to made about their composition. Currently, there is very little evidence for the existence of filaments, with most studies focusing on individual filaments between rich cluster.

Dietrich et al. (2012) reported the detection of a dark matter filament connecting massive clusters, Abell 222 and Abell 223, using weak lensing. They ruled out the possibility of the system being a cluster triplet by comparing two parametric models, one with the cluster triplet with a filament and the other with two clusters and a filament. In order to find cluster masses consistent with previous studies they required the halo concentration to be a free parameter in a fit to an NFW profile (Navarro et al., 1997), giving both roughly the same mass of $\sim 2 \times 10^{14} M_\odot$. They found that the surface density of the filament was significantly higher than expected, which they attribute to the filament major axis being along the line-of-sight. The mass of the filament from a non-parametric reconstruction was found to be consistent with the parametric fit, at $M_{\rm fil} = 6.5 \pm 0.1 \times 10^{13} M_\odot (9.8 \pm 4.4 \times 10^{13} M_\odot)$ with a significance of 4.1σ.

More recently, Higuchi et al. (2015) reported the detection of a filament between galaxy clusters CL0015.9+1609 and RX J0018.3+1618. They constrained the cluster masses using galaxy-galaxy lensing, finding the virial masses to be $M_{\rm vir} = 2.09^{+0.10}_{-0.21} \times 10^{15} h^{-1} M_\odot$ and $M_{\rm vir} = 4.51^{+1.13}_{-1.05} \times 10^{14} h^{-1} M_\odot$, respectively. They subtracted the cluster contributions using an NFW profile as a model of the cluster shears, but also empirically using the outside regions of the clusters, finding a filament surface mass density of $\Sigma_{\rm fil} = 3.20 \pm 0.10 \times 10^{14} h M_\odot {\rm Mpc}^{-2}$ at $\sim 2\sigma$ significance.

These individual filament detections rely on a more or less arbitrary parametric filament model. When stacking many filaments together the signal becomes statistical in nature

and an improved model for the stacked filament may be in higher order perturbations, *i.e.*, the three-point correlation function. In particular, one wants to look between massive groups and clusters of galaxies, as mentioned above. Without any information about the groups and clusters, a proxy for their centers are luminous red galaxies (Hoshino et al., 2015).

The three point galaxy-galaxy-shear correlation function from weak lensing was investigated by Simon et al. (2013) using the CFHT Lensing Survey, where they looked at the excess surface mass density around stacked galaxy pairs, both early-type and late-type, as a measure of the galaxy-galaxy-matter bispectrum. They report an excess of surface density, almost exclusively around early-type galaxies, with the excess around late-types being consistent with null. The report of an excess around early-types is to be expected in the context of filaments, however their use of photometric redshifts to identify pairs of galaxies would be cause for concern. The relatively large error in photometric redshifts (~ 0.05 or $150h^{-1}$Mpc) will almost certainly scatter physically connected pairs of galaxies away, and scatter seemingly independent galaxies together, as will be mentioned in §2.1.2.

A study of filaments in the context of the three-point correlation function by Clampitt et al. (2014) investigated the weak lensing signal between SDSS Luminous Red Galaxies (LRGs) at various separations. Their study is restricted SDSS which has the benefit of spectroscopic redshift data for their LRGs. The use of SDSS source galaxies may be prone to systematics than other surveys, such as point-spread function modelling as well as the relatively shallow depth. They presented two filament models, one based on the three-point correlation function, and the other a string of NFW halos. The data are in favour of the model based on the correlation function, yielding a 10σ filament detection, however to fit the data they required the model to be scaled down, with no obvious reason. Using this model fit, they estimated the mass of the filaments as a function of radius, giving masses on the order of $10^{14} - 10^{15} M_{\odot}$. Since they found the model overpredicted the signal by factor of ~ 10 times, it needed to be scaled down in order to fit the data. As such, the results should be interpreted with caution.

In this work, we are concerned with the development of techniques needed to measure the filament signal between groups and clusters, and also the attempt to accurately model this signal using the three-point correlation function. The use of the three-point correlation function as a model is the simplest, and from its definition, the (current) best theoretical description for a mass bridge between two massive halos. One major complication present when dealing with higher order perturbations in linear theory is that they don't have a clear interpretation in the context of filaments. Furthermore, as you move to the non-linear

regime, the subsequent orders becomes equally, if not more, important. For this work, we don't consider the possibility of higher order correlations, however they should be kept in mind.

1.4 Thesis Summary

In this work we develop the tools and techniques needed to use weak lensing as a method to detect the filamentary structure predicted in simulations. The methods presented in this work will serve as a baseline for future lensing surveys, making it possible to detect filaments with ease.

In Chapter 2 we discuss the use of CFHTLenS for galaxy source shapes and photometric redshifts, and SDSS for a catalogue of candidate groups and clusters with spectroscopic redshifts. A method of stacking filaments at random orientations and varying lengths is developed in order to combine the signal from many. The stacking procedure is outlined, and the results are presented in both shear and convergence maps. Techniques to isolate the filament signal from the shear signal of the individual clusters are presented: the subtraction of non-physical pairs, and the subtraction of outside regions of LRGs. Finally we present an empirical measurement of the stacked filament surface mass density and total mass.

In Chapter 3 we develop the model for filaments in the context of the perturbation theory three point correlation function, starting from the definition of the three-point galaxy-galaxy-convergence correlation function. At the end of the chapter we present the comparison of the data in convergence-space, employing the methods of isolating the filament signal presented in Chapter 2. We discuss the comparisons, and mention possible improvements to the model.

In Chapter 4 we summarize the the results of the study, comparing with previous studies, and discussion possible improvements. We conclude with a discussion of this work in a broad context, the application of weak lensing in future dark matter filament searches, and upcoming surveys.

Throughout this work we adopt a cosmology with the following parameters: $\Omega_{\mathrm{m}} = 0.3$, $\Omega_{\Lambda} = 0.7$, $h \equiv H_0/(100\mathrm{km\,s}^{-1}\mathrm{Mpc}^{-1}) = 0.7$, $n_s = 0.96$, and $\sigma_8 = 0.8$.

Chapter 2

Measurement of Filament Signal

In this chapter we present the data and techniques used to produce a weak lensing signal of between LRG pairs, and methods of isolating any filament signal. §2.1 is an overview of the surveys used for lens and source catalogues while §2.2 introduces the technical details of getting the shear signal from the lens-source system. In §2.3 we present two methods of isolating the filament signal from the LRGs, and in §2.4 we present the resulting empirical convergence and mass of the stacked filament.

2.1   Observational Data

In order to study the weak lensing signal of filaments one requires two sets of data: A catalogue of galaxy groups and cluster pairs, and a catalogue of background galaxies with accurate shape measurements. The spectroscopic redshifts available from the Sloan Digital Sky Survey (SDSS) are essential for finding for a catalogue of galaxy groups and cluster pairs, and the source shapes from the Canada France Hawaii Telescope Lensing Survey (CFHTLenS) are the best available to date with accurate shape measurements for millions of galaxies and deep i-band photometry over 150 square degrees. As such these are the two surveys used in this study.

2.1.1   CFHTLenS

As mentioned in §1.2, weak lensing is the regime of gravitational lensing in which the shapes of background galaxies are distorted according to a foreground lens. In any study

of weak lensing, one requires accurate shape measurements to measure the effect of the lens. This is especially important in the study of filaments because this distortion is significantly smaller than a galaxy or galaxy cluster. CFHTLenS provides the best weak lensing catalog in this regard, having accurate shape measurements for more than 10^6 galaxies, with deep i-band photometry, down to a magnitude of 24.7.

The CFHTLenS data set is derived from the Canada France Hawaii Telescope Legacy Survey (CFHTLS), optimized for weak lensing measurements. Observations were made between March 2003 and November 2008 with the CFHT MegaPrime instrument (roughly a $1° \times 1°$ field of view) mounted on the telescope. The measurements were taken in four patches on the sky: W1 with 72 fields around $\alpha = 34.5°, \delta = -7.00°$, W2 with 33 (only 25 used) fields around $\alpha = 34.5°, \delta = -7.00°$, W3 with 49 fields around $\alpha = 214.48°, \delta = 54.51°$, and W4 with 25 fields around $\alpha = 333.33°, \delta = 1.32°$. CFHTLenS uses five optical filters $u^* \ g' \ r' \ i' \ z'$ and covers ~ 154 square degrees with 17 resolved galaxies per square arcmin (Erben et al., 2013).

Galaxy shape measurements were made using the '*lensfit*' algorithm, modelled with bulge and disk components ultimately giving the two ellipticity parameters, e_1 and e_2 by bayesian marginalization over galaxy size, centroid and bulge fraction. A corresponding *lensfit* weight was assigned to each galaxy given the variance of the ellipticity likelihood surface defined in equation 8 of Miller et al. (2013)(Miller et al., 2013; Heymans et al., 2012).

Photometric redshifts (photo-zs) were estimated using the Bayesian Photometric Redshift (BPZ) Code outlined in Benítez (2000), making use of the five colour filters available from CFHTLS (Hildebrandt et al., 2012), yielding a mean photometric redshift of 0.75, much deeper than the lens sample of ~ 0.4. The photo-zs are limited to the range $0.2 < z_{phot} < 1.3$, with an average scatter of $\sigma_z \sim 0.04(1 + z)$ and a catastrophic outlier rate of $\lesssim 4\%$ (Heymans et al., 2012). For a detailed description of the methods used to estimate the photo-zs see Hildebrandt et al. (2012).

2.1.2   SDSS

Filaments intersect the high density nodes in N-body simulations where galaxy groups and clusters will be forming and as such, it is expected that the filaments exist between pairs of galaxy groups and clusters. To identify pairs of galaxy groups and clusters that are connected by a filaments, one requires an accurate estimate of their location in redshift space. Unfortunately, the uncertainty associated with photometric redshifts, as measured

18

in CFHTLenS, will scatter true pairs away from each other and scatter false pairs to the same redshift. For example, if there are two galaxy clusters separated by a photometric redshift of $\Delta z_{\mathrm{phot}} = 0.05$ (the minimum photometric redshift separation in CFHTLenS), the uncertainty in their line-of-sight separation, if only due to Hubble flow, would be $\sim 150 h^{-1}\mathrm{Mpc}$. In order to mitigate this issue, pairs should be identified with spectroscopic redshifts, which have orders of magnitude better redshift accruacy ($\sigma_{z_{\mathrm{spec}}} \sim 10^{-4}$). For comparison, the same calculation with the spectroscopic redshifts gives a conservative uncertainty in separation of roughly $0.3 h^{-1}\mathrm{Mpc}$. This is much smaller than the scales with which we are concerned in this study.

SDSS is an excellent survey in this regard as it has spectroscopy for its galaxies and sufficiently large overlap with CFHTLenS in its most recent release, particularly the Baryon Oscillation Spectroscopic Survey (BOSS). What makes BOSS a useful program for our purposes (as well as its primary goal of measuring the BAO scale) is that it was targeted specifically at Luminous Red Galaxies (LRGs), an excellent proxy for the centers of galaxy groups and clusters.

SDSS is the largest redshift survey to date, having gone through three major project phases, conveniently named SDSS-I (2000-2005), SDSS-II (2005-2008), and SDSS-III (2008-2014). Data Release 12 (DR12) is the final data release from SDSS-III containing all observations up to July 2014, including the complete BOSS data sets. In this study the BOSS CMASS and LOWZ galaxies were selected using the color-magnitude cuts from Dawson et al. (2013) and chosen such that they overlapped the CFHTLenS area. The majority of the overlap is over the W1 patch in CFHTLenS, however with the release of DR12 the W3 and W4 patches have filled in substantially (leaving W2 with very little overlap), in total giving $\sim 24,000$ LRGs in total.

A catalogue of LRG pairs was constructed from the BOSS galaxy overlap by selecting pairs that were separated in redshift by $\Delta z_{\mathrm{spec}} < 0.002$, and subsequently binned into projected physical separation bins ($6 h^{-1}\mathrm{Mpc} \leq R_{\mathrm{sep}} < 10 h^{-1}\mathrm{Mpc}$). This gave a sample of $\sim 23,000$ pairs of LRGs, with a mean physical separation of $\langle R_{\mathrm{sep}} \rangle \sim 8.23 h^{-1}\mathrm{Mpc}$ with mean redshift $\langle z \rangle \sim 0.42$, a mean stellar mass of $\langle \log_{10} M_\star / M_\odot \rangle \sim 11.3$.

2.2 Lensing Shear Signal

Unlike galaxy-galaxy lensing where one is often interested in the circularly averaged *tangential* shear around individual galaxy centers, measuring the shear signal around pairs of LRGs is more complicated. The main complication comes from non-linear structure not necessarily being spherically symmetric, producing a shear signal that is not purely tangential. It is crucial then to have a method of stacking the lens-source system that can keep track of both components of the shear, γ_1 and γ_2. In addition one needs to develop a way to account for the random orientations of LRG pairs, and their variable separation length. In §2.2.1 below we develop a standard coordinate system that allows for the stacking of arbitrary orientations and length, and in §2.2.2 the actual stacking procedure is outlined.

2.2.1 Standardized Coordinates

If this were galaxy-galaxy lensing it would be as simple as binning in radial annuli around the lens centre, however there are two key differences to keep in mind for the LRG pair system: pairs of LRGs on the sky appear to have uniform random orientations relative to the background galaxies (see Figure 2.1), and they have varying physical separations. To take care of this we define what will be referred to as a *standardized* coordinate system.

This standardized coordinate system is normalized by pair separation, R_{sep}, and rotated such that the LRG pair coordinates will translate to $(x_L, y_L) = (-0.5, 0)$ and $(x_R, y_R) = (0.5, 0)$. In order to have a sensible lensing signal, the source galaxy's positions and shape ellipticities must also be translated into this coordinate system:

1. First the galaxy's position is translated such that the central right ascension and declination, (α_c, δ_c), of the LRG pair is at the origin, then projected into the tangent plane of the central point,

$$\begin{aligned} X'_{\text{g}} &= -(\alpha_{\text{g}} - \alpha_{\text{c}}) \cos \delta_{\text{c}} \\ Y'_{\text{g}} &= \delta_{\text{g}} - \delta_{\text{c}}. \end{aligned} \tag{2.1}$$

2. Next the coordinates are rotated such that the LRG pair lies along the x-axis. This is done using the rotation matrix,

$$R = \begin{bmatrix} \cos \theta & \sin \theta \\ -\sin \theta & \cos \theta \end{bmatrix}, \tag{2.2}$$
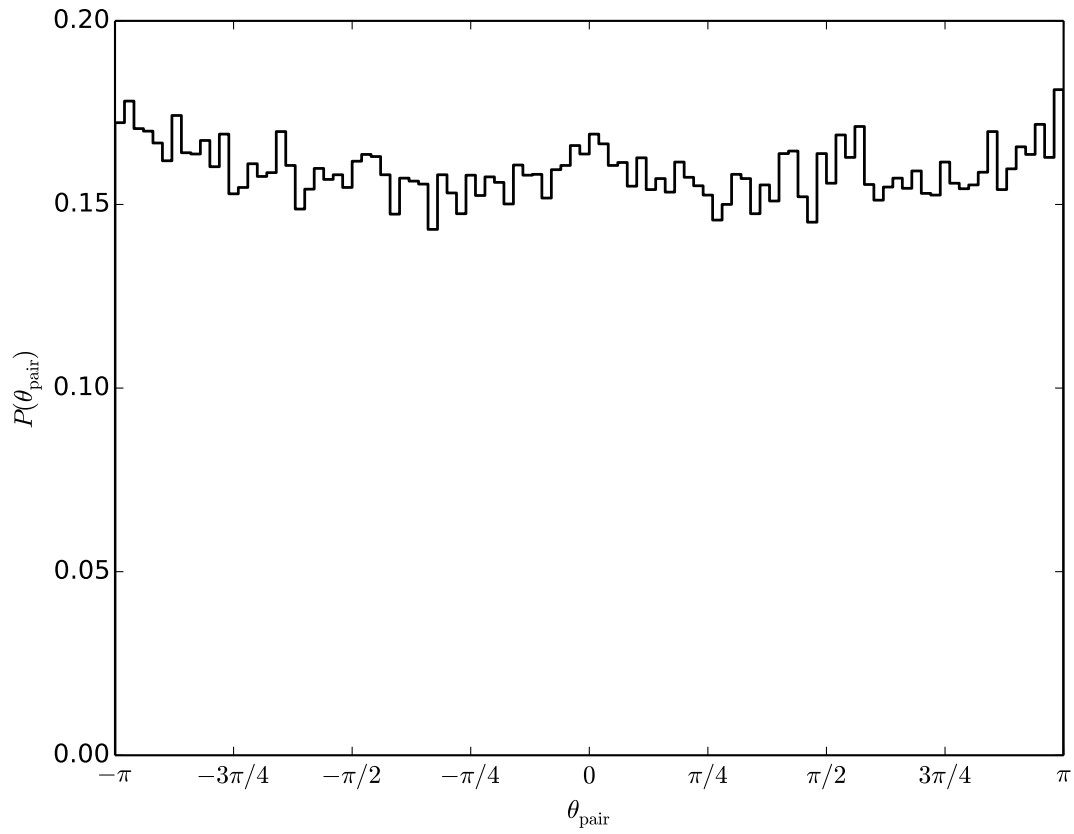
Figure 2.1: The distribution of LRG pair angles, θ, as measured in the tangent plane projection relative to the X-axis see (2.3). It is clear that the LRGs are distributed uniformly from $(-\pi, \pi)$

21

where θ is the angle between the individual LRGs about the central point in the tangent plane,

$$\theta = \tan^{-1}\left(\frac{Y'_R - Y'_L}{X'_R - X'_L}\right). \tag{2.3}$$

The subscripts L, R represent the "left" and "right" LRGs in the pair.

3. Finally the coordinates are rescaled by the separation between the two LRGs in the tangent plane,

$$s = \sqrt{(\alpha_R - \alpha_L)^2 \cos^2 \delta_c + (\delta_R - \delta_L)^2}. \tag{2.4}$$

This is the angular separation that corresponds to a projected physical separation, R_{sep}.

Putting it all together, the final position of a galaxy in this coordinate system will be,

$$
\begin{aligned}
x_{\mathrm{g}} &= \frac{1}{s}\left[(\alpha_{\mathrm{c}} - \alpha_{\mathrm{g}})\cos\delta_{\mathrm{c}}\cos\theta + (\delta_{\mathrm{g}} - \delta_{\mathrm{c}})\sin\theta\right] \\
y_{\mathrm{g}} &= \frac{1}{s}\left[-(\alpha_{\mathrm{c}} - \alpha_{\mathrm{g}})\cos\delta_{\mathrm{c}}\sin\theta + (\delta_{\mathrm{g}} - \delta_{\mathrm{c}})\cos\theta\right]
\end{aligned}
\tag{2.5}
$$

With the source galaxies in the new coordinate system, their ellipticities also need transformed. Fortunately, the ellipticity isn't defined relative to any particular point on the sky so the 2 components of ellipticity only need to be rotated, not translated or rescaled. The rotation matrix is nearly the same as (2.2), however the property that ellipticity is invariant under 180° rotation requires that the angle just be doubled,

$$
\begin{aligned}
e'_1 &= e_1 \cos 2\theta + e_2 \sin 2\theta \\
e'_2 &= -e_1 \sin 2\theta + e_2 \cos 2\theta
\end{aligned}
\tag{2.6}
$$

2.2.2 Stacking

The signal from an individual filament is expected to be very small as their density is much smaller than that of a galaxy or cluster of galaxies. In order to study the filaments of many LRG pairs we take an ensemble average, known as 'stacking'.

In order to stack the source shapes around a pair of LRGs (from here on referred to as a 'lens'), a two dimensional grid is prepared, as in Figure 2.2, based on the $x - y$ coordinate system developed in §2.2.1. For each lens, at all (x, y) cells of the grid, the the shear components are computed by averaging the source galaxy shapes (e_1 and e_2) according to

22

their *lensfit* weights, w, with an additional factor of $\Sigma_{\text{crit}}^{-2}$ as in Hudson et al. (2015). The additional factor of $\Sigma_{\text{crit}}^{-2}$ is used to down-weight sources that are near the lens in redshift, for which the signal is expected to be very weak. The critical surface density, Σ_{crit}, is given by (1.12)

$$\Sigma_{\text{crit}}(z_\ell, z_j) = \frac{c^2}{4\pi G}\frac{D(z_j)}{D(z_\ell)D(z_\ell, z_j)}, \tag{2.7}$$

where $D(z_\ell)$ is the angular diameter distance to the lens, $D(z_j)$ is the angular diameter distance to the source, and $D(z_\ell, z_j)$ is the angular diameter distance between the lens and source. To summarize, the shears are stacked according to

$$
\begin{aligned}
\gamma_1(x, y) &= \frac{\sum_\ell \sum_{j\in(x,y)} e'_{1,j} w_j \Sigma_{\text{crit};\ell,j}^{-2}}{\sum_\ell \sum_{j\in(x,y)} w_j \Sigma_{\text{crit};\ell,j}^{-2}} \\
\gamma_2(x, y) &= \frac{\sum_\ell \sum_{j\in(x,y)} e'_{2,j} w_j \Sigma_{\text{crit};\ell,j}^{-2}}{\sum_\ell \sum_{j\in(x,y)} w_j \Sigma_{\text{crit};\ell,j}^{-2}},
\end{aligned}
\tag{2.8}
$$

where the average is over all lenses, ℓ, and background sources, j, that belong to cell (x, y) after the coordinate transformation. An additive correction is applied to the e_2 component (before rotating) when computing the shears, according equation (19) of Heymans et al. (2012), that accounts for a bias in CFHTLenS lensfit shape measurement that has an unclear origin. Additionally, Miller et al. (2013) found that a multiplicative correction for noise bias needs to be applied *after* the shapes are stacked, calculated from

$$1 + K = \frac{\sum_\ell \sum_j \left[1 + m(\nu_{SNR}, r_{\text{gal}})_j\right] w_j \Sigma_{\text{crit};\ell,j}^{-2}}{\sum_\ell \sum_j w_j \Sigma_{\text{crit};\ell,j}^{-2}}. \tag{2.9}$$

The resulting corrected shears are then

$$\gamma_{1,2}^{\text{cor}}(x, y) = \frac{\gamma_{1,2}(x, y)}{1 + K}. \tag{2.10}$$

In principle, one can stack any quantity according to this prescription to get the ensemble average over the entire field. For some arbitrary quanitity, Z, the averaged over the entire field would be

$$Z = \frac{\sum_\ell \sum_j Z_{\ell,j} w_j \Sigma_{\text{crit};\ell,j}^{-2}}{\sum_\ell \sum_j w_j \Sigma_{\text{crit};\ell,j}^{-2}}. \tag{2.11}$$
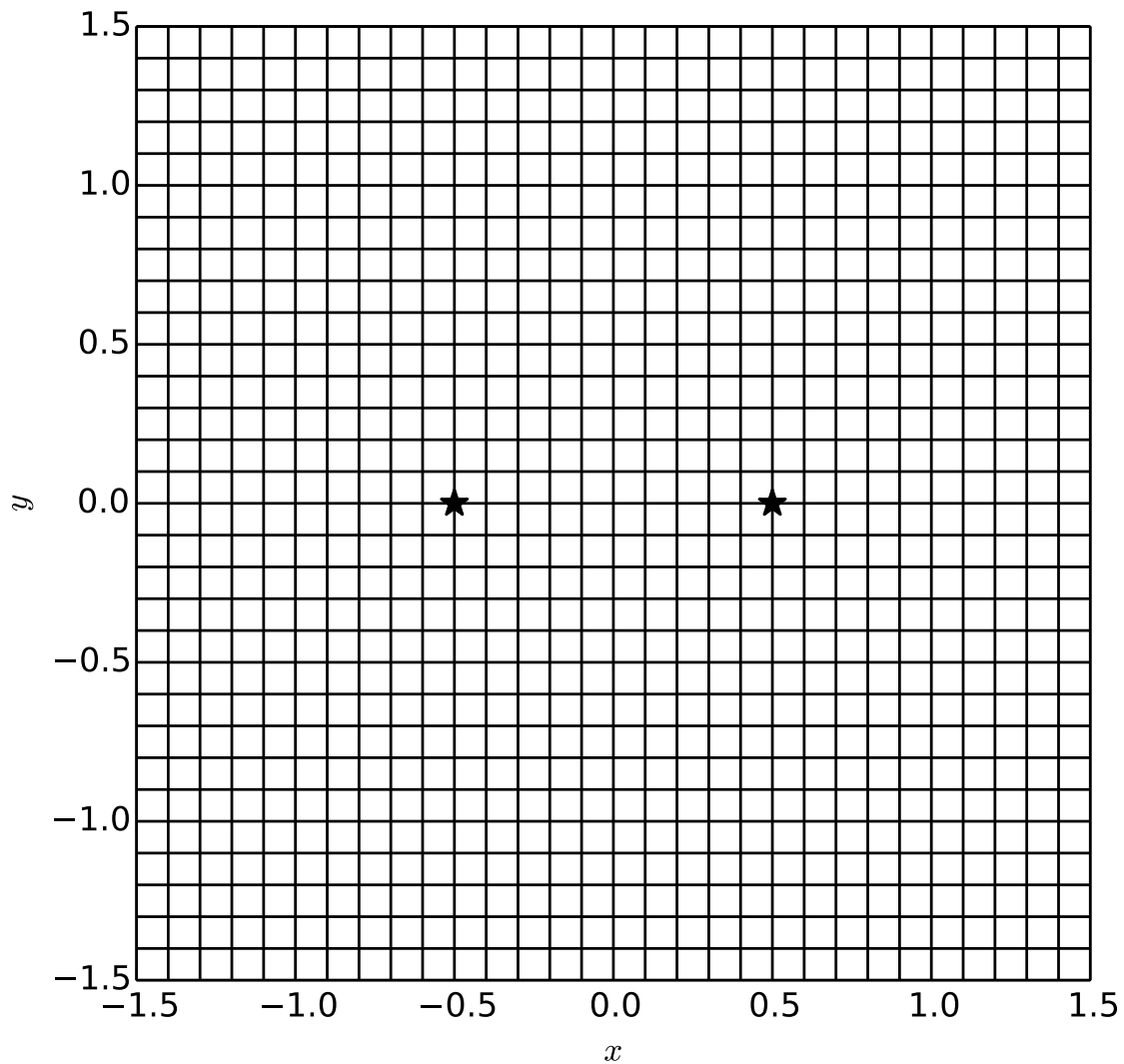
Figure 2.2: The grid in which the background galaxy shapes are to be stacked in the standardized coordinate system. For the purpose of illustration this particular grid is more coarse than what's used in the lensing measurements. The LRG positions are marked at $x = \pm 0.5$.
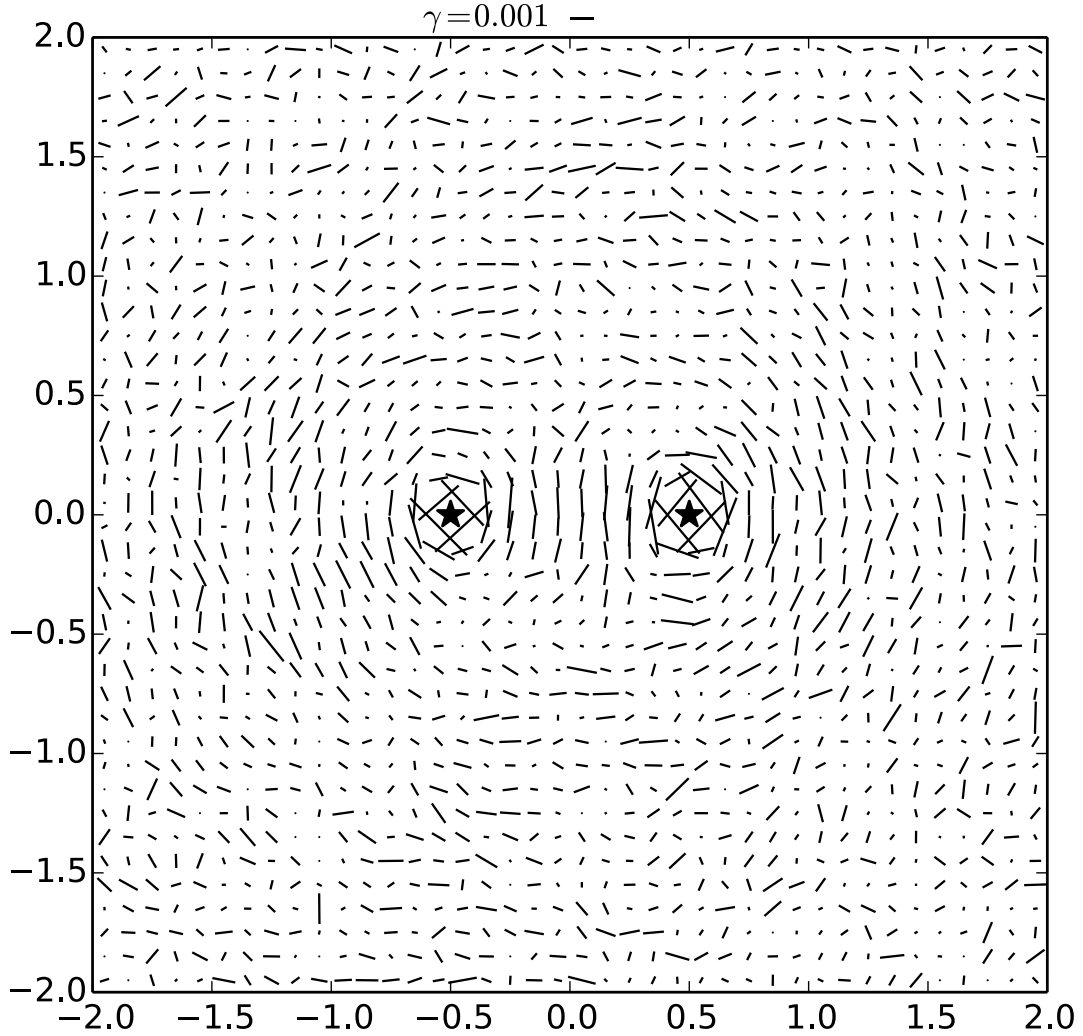
Figure 2.3: The resulting shear map after stacking background galaxy shapes for LRG pairs in the projected physical separation bin $6h^{-1}\mathrm{Mpc} < R < 10h^{-1}\mathrm{Mpc}$. The shears have been re-binned into a coarse grid for the purpose of illustration. The tangential nature of the shears around the LRGs is clearly visible.

25

2.2.3   Convergence & Surface Mass Density

One problem with examining shears directly is that they are difficult to interpret. In the case of galaxy-galaxy lensing, one can interpret the tangential shear as the mean excess mass density, however there is no analogous comparison with the individual shear components. Using the method of Kaiser & Squires presented in §1.2.2 the shears in Figure 2.3 can be inverted to get a convergence map by solving (1.19), giving a more easily interpreted map of the lens surface density. An example of the convergence map is shown for the separation bin $6h^{-1}\mathrm{Mpc} \leq R_{\mathrm{sep}} < 10h^{-1}\mathrm{Mpc}$ in Figure 2.4.

From the definition of convergence, we easily convert to the surface mass density

$$\Sigma = \kappa \overline{\Sigma}_{\mathrm{crit}}, \tag{2.12}$$

where $\overline{\Sigma}_{\mathrm{crit}}$ is the ensemble average, calculated using (2.11),

$$\overline{\Sigma}_{\mathrm{crit}} = \frac{\sum_\ell \sum_j \Sigma_{\mathrm{crit};\ell,j} \cdot \Sigma_{\mathrm{crit};\ell,j}^{-2} w_j}{\sum_j w_j \Sigma_{\mathrm{crit};\ell,j}^{-2}}. \tag{2.13}$$

The mean $\overline{\Sigma}_{\mathrm{crit}}$ was found to be $1637.36 M_\odot/\mathrm{pc}^2$ for our sample.

2.3   Isolating The Filament Signal

In order to compare the filament signal to model predictions, the shear contribution from the two LRGs must be removed. Simulations suggest that the halo LRGs live in will likely be an NFW profile or some extension of the NFW (Navarro et al., 1997). A single halo may not be spherically symmetric, but an ensemble average over many halos is expected to be and as noted in §1.2.1, a spherically symmetric lens will produce purely tangential shears. One requires a method that will remove any tangential shear produced by the LRG halos, leaving behind a signal only from the filament. Here we present two model independent methods of removing the LRG lensing signal from the data.

2.3.1   Non-Physical Pair Subtraction

A particular pair of LRGs that are thought to be physically connected is identified based on their separation in redshift such that their line-of-sight separation is minimized. This same
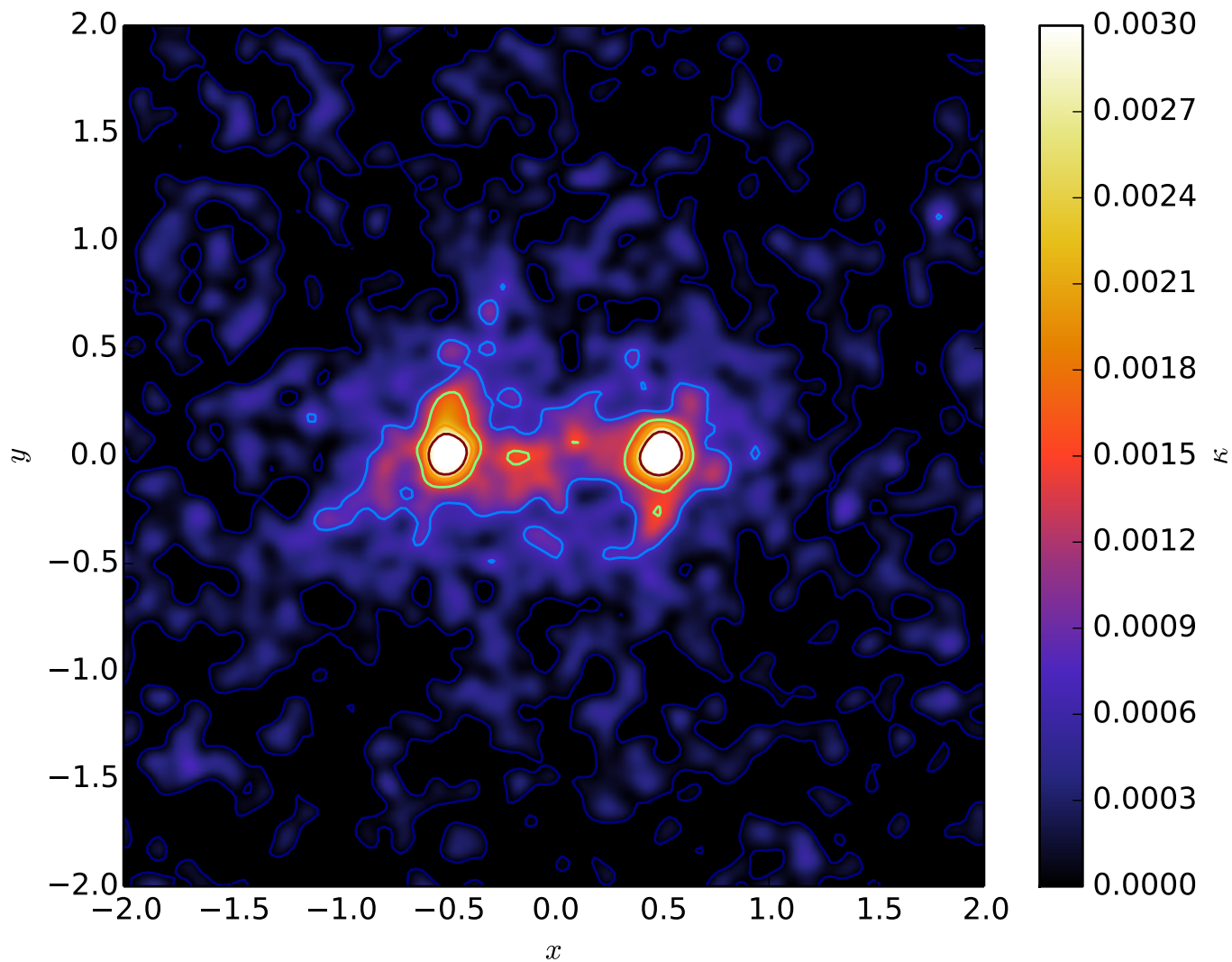
Figure 2.4: The convergence, κ, map obtained from applying the Kaiser & Squires inversion (§1.2.2) on the shears in Figure 2.3, in finer grid. For the purpose of illustration a gaussian smoothing filter of width 0.04375 in units of x, y has been applied. There is a clear sign of a mass bridge between the two LRGs.

approach can be used to find pairs that fall into a particular projected separation bin, but have such a large line-of-sight separation that the probability of being connected by a filament is negligible. These clusters are said to be not physically associated with one another.

Non-physical pairs of LRGs are selected to be between line-of-sight separation between $100h^{-1}\mathrm{Mpc}$ and $120h^{-1}\mathrm{Mpc}$ corresponding to a separation in redshift of $0.033 \lesssim \Delta z \lesssim 0.04$. For determining background sources, we assume that the lens redshift is the average of the pair. The resulting shears from the non-physical pairs being stacked should only have contributions from the two LRGs, so a direct subtraction should give a residual filament signal. With this method the data can be compared to the model with relative ease in either shear-space or convergence space. Since it is easier to interpret the signal in convergence space we do all analysis in convergence space. Figure 2.5 shows the convergence map from the lensing signal for pairs of clusters that are not physically associated with each other in the projected separation bin $6h^{-1}\mathrm{Mpc} \leq R_{\mathrm{sep}} < 10h^{-1}\mathrm{Mpc}$. A key feature of Figure 2.5 is the lack of of bridge between the two LRGs that is seen in Figure 2.4.

2.3.2 Outside Region Subtraction

An alternative method to subtracting the unphysical pairs is to use the outer regions of the LRG pairs to empirically subtract off the total LRG component of the signal. The motivation for this method is that we expect the LRG to have a roughly circularly symmetric component on the outer regions. Since the filament is assumed to exist only between the LRG pair, the outside region should remove any circularly symmetric contribution of the LRG from the inner filament region.

For this method, we choose a width for the filament, Δy, and compute the mean convergence within a vertical bar along the x-axis. The outside regions are then mirrored to the inside region, and subtracted from the total signal. Figure 2.6 schematically shows how the outer regions of the LRGs are subtracted from the inner regions. The peaks at $x = \pm 0.5$ are from the LRG signal, and it should be noted that there is a slight asymmetry about the peak centre. For a spherically symmetric LRG we would expect this peak to be symmetric. To avoid this asymmetry influencing any filament signal, all comparisons are made avoiding the regions closest to the LRG centers.
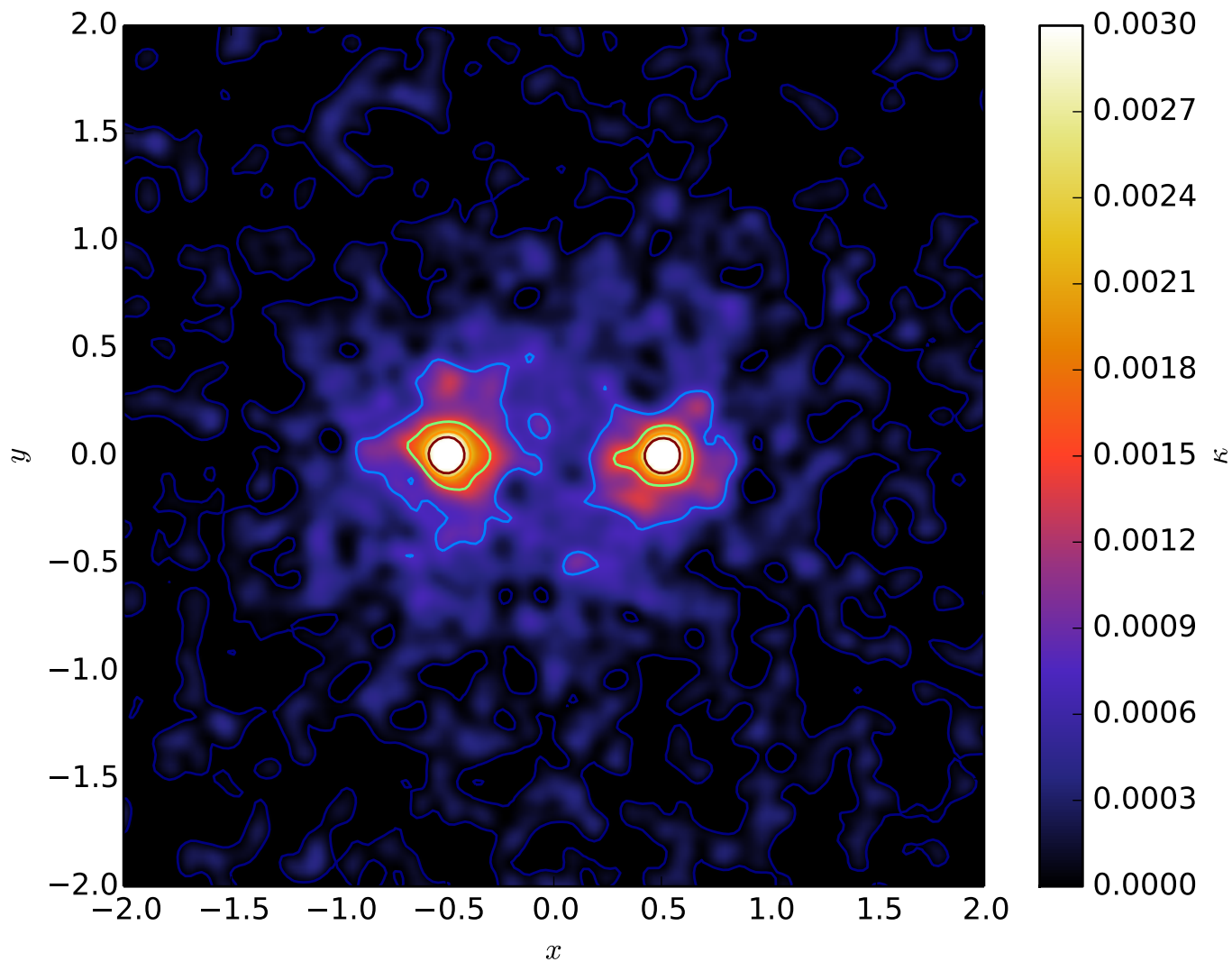
Figure 2.5: The same as Figure 2.4, but for the non-physical pairs of LRGs. The non-physical pairs lack the apparent filamentary feature between the LRGs that is clear in Figure 2.4. For the purpose of illustration a gaussian smoothing filter of width 0.04375 in units of x, y has been applied.
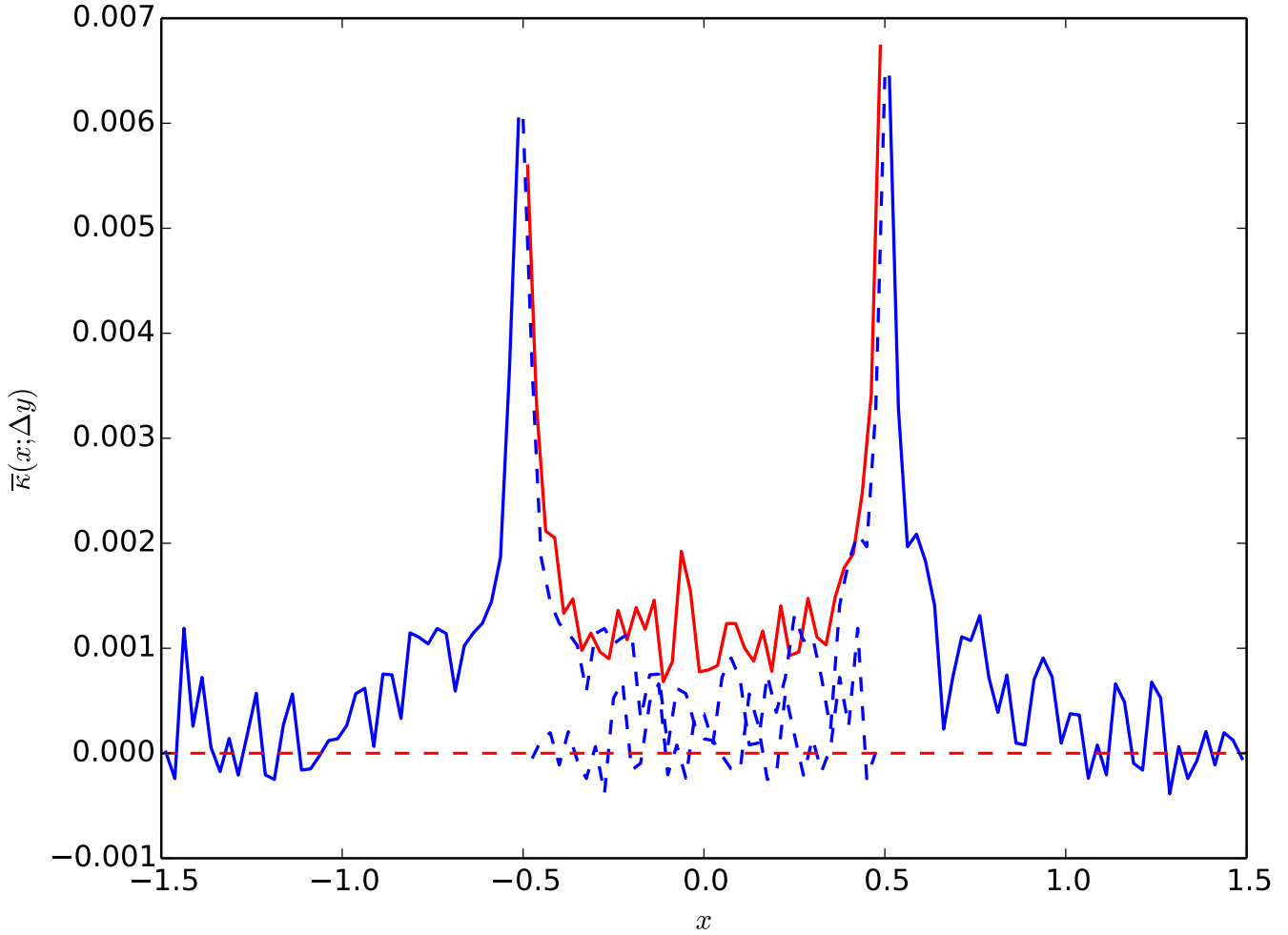
Figure 2.6: A schematic for how the outer regions of the LRGs are subtracted from the inner regions for a fixed filament width Δy. The blue dashed lines show the mirrored imaged of the of outside regions from $x = \pm 1.5$ to ± 0.5, overlaid in the centre. This particular Δy is for the fiducial width described in §2.4

2.4   Results

Figure 2.4 shows the resulting convergence map after stacking pairs of LRGs between $6h^{-1}$Mpc and $10h^{-1}$Mpc. The striking feature of Figure 2.4 is a clear structure connecting the two LRGs is apparent. This is what we take to be the stacked filament connecting the LRGs. We would like to empirically estimate the mass, without relying on any model fits. This poses two problems: what constitutes the filament region, and how can we separate the filament from the LRG signal, without removing the any additional filament signal. For our purposes, we consider the filament to be anything beyond the contribution from the LRGs and we isolate the signal according to the methods above.

The statistical properties of the filament are expected to be described by the three-point correlation function. The three-point function predicts an excess mass density on the outside regions of the LRGs so the method of subtracting outer regions will in principle remove parts of the filament signal. We expect the non-physical pairs to be completely independent of each other having no connecting large-scale structures, and as such the resulting shear and convergence should only be the superposition of LRG signals. Performing a direct subtraction will more than likely have small over or under subtraction of the convergence in the regions closest to the LRG positions due to a small difference in the physical and non-physical pair masses. Furthermore, some studies suggest that the the typical r_{200} of a dark matter halo may not be the optimal boundary (More et al., 2015a), with accreting matter extending as far as $1.5r_{200}$. To avoid including these effects in the mass estimate, data is only considered outside $2r_{200}$ from either LRG, avoiding any contributions from the LRG halo.

To measure the residual filament signal, we start by subtracting the convergence map in Figure 2.5 from the convergence map in Figure 2.4. We place a box of dimensions $\Delta x \times \Delta y$, representing the projected dimensions of the stacked filament (See Figure 2.7), and measure the average convergence contained inside the box. The typical r_{200} of the LRG halo is estimated using the stellar-to-halo mass ratio from Hudson et al. (2015) for red galaxies with stellar mass $\sim 10^{11.3} M_\odot$ and redshift ~ 0.4, giving and $r_{200} \sim 400$kpc. r_{200} is converted into x_{200} by normalizing to the pair separation R_{sep}, $i.e.$, $x_{200} = r_{200}/R_{\text{sep}} \sim 0.035$. $2x_{200}$ is roughly 3 bins away from the left and right LRGs, so for all analysis we do not consider these 6 bins.

Figure 2.8 shows the resulting average convergence as the width of the box, Δy, is increased. From the convergence we converted to a surface mass density using (2.12). It is
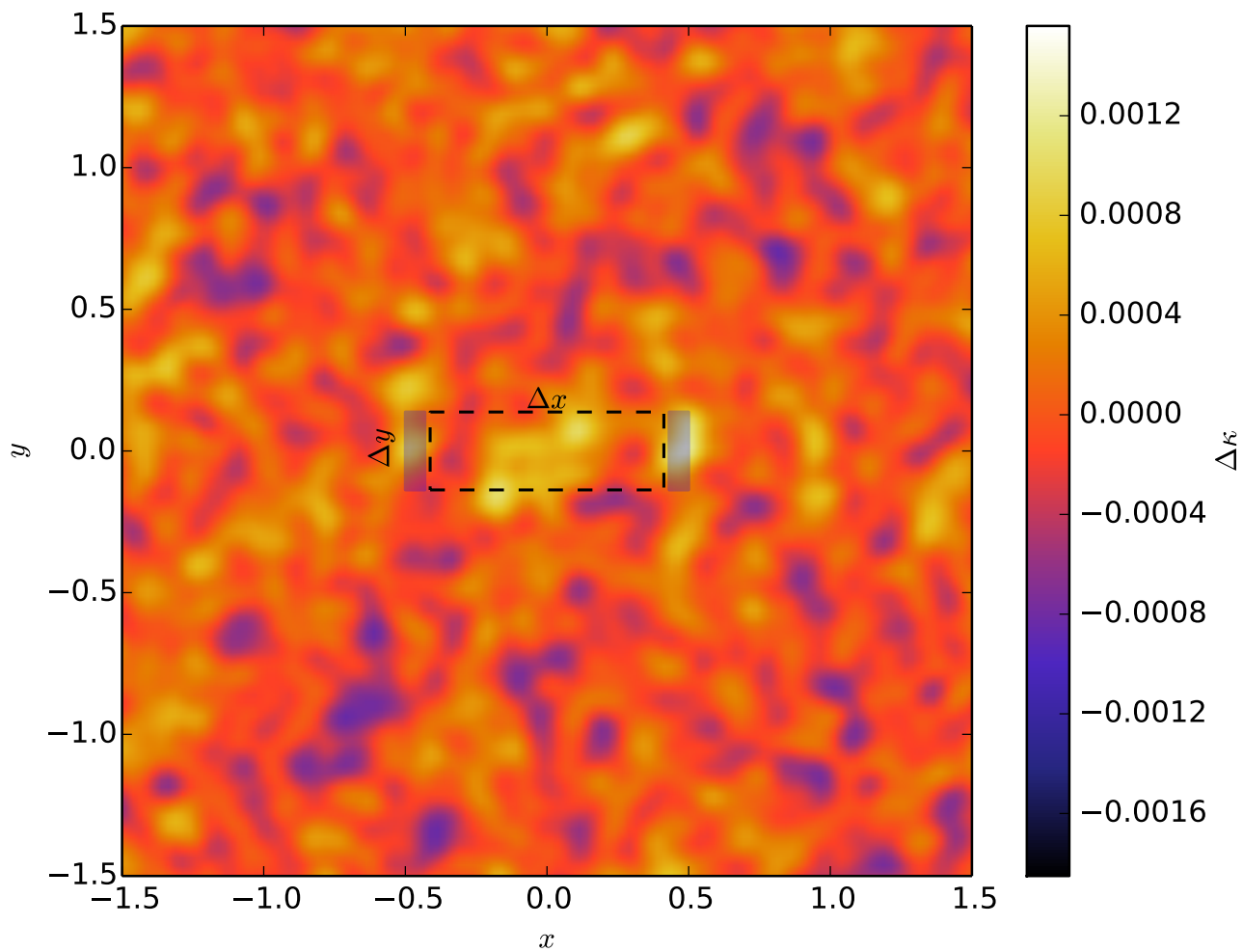
Figure 2.7: The result of subtracting the non-physical pair convergence from the physical pairs. The shaded regions indicate where the regions within the LRG halos are excluded from the filament measurement. Δx is fixed for all measurements, however Δy varies, mapping out the convergence as a function of filament width, see Figure 2.8. A gaussian smoothing filter is also applied for the purpose of illustration.

32

Figure 2.8: The resulting average convergence within a box of dimensions $\Delta x \times \Delta y$. The function is monotonically decreasing.

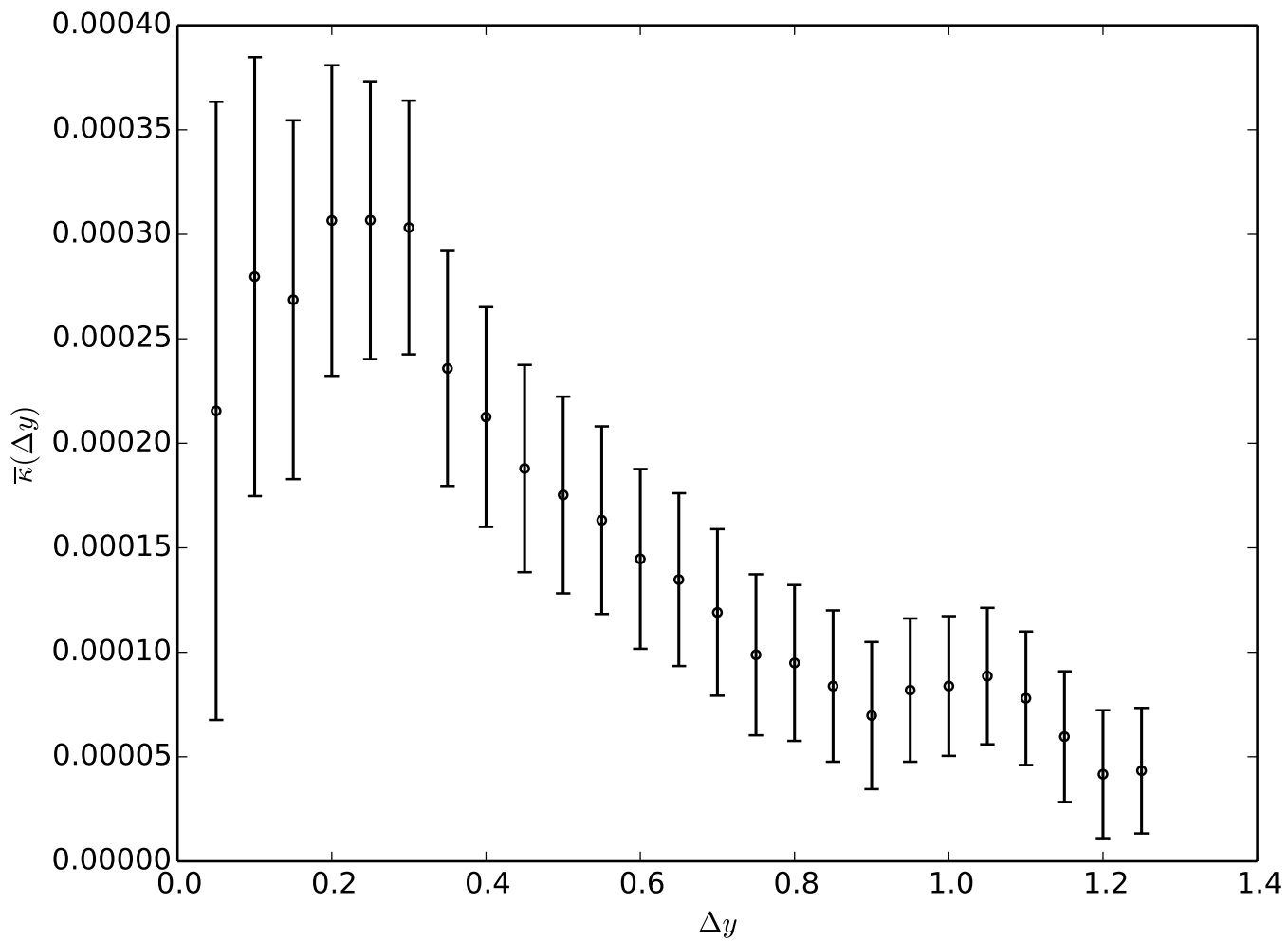then straightforward to calculated the average mass contained within the filament box, shown in Figure 2.9. From Figure 2.8, we see that the signal-to-noise peaks around $\Delta y = 0.3$ corresponding to a physical width of $2.47h^{-1}$Mpc at a significance of $\sim 5\sigma$. The corresponding mass contained within the filament is $\overline{M}_{\rm fil} = (1.6 \pm 0.3) \times 10^{13}M_{\odot}$. We see that the filament mass shows no sign of increasing beyond this Δy so we adopt $2.47h^{-1}$Mpc as the fiducial width.

The filament mass is on the same order as reported by Dietrich et al. (2012), but about one order of magnitude smaller than the mass of the filament reported by Higuchi et al. (2015). The discrepancy in mass is more than likely due to the typical halo masses considered in this work, the average halo mass being on the order of $\sim 10^{13}M_{\odot}$ which would correspond to a rich group rather than a massive cluster. The halos considered in Higuchi et al. (2015) on the other hand are greater than $10^{14}M_{\odot}$, housing a rich cluster of galaxies. An alternative explanation, albeit undesirable is that the sample of LRGs is contaminated. According to Hoshino et al. (2015), the fraction of BOSS LRGs that do not belong to the centre of a galaxy group or cluster can possibly be as high as 30%. This would introduce noise into the shears in the filament region, and the resulting surface density reconstruction would be diluted.
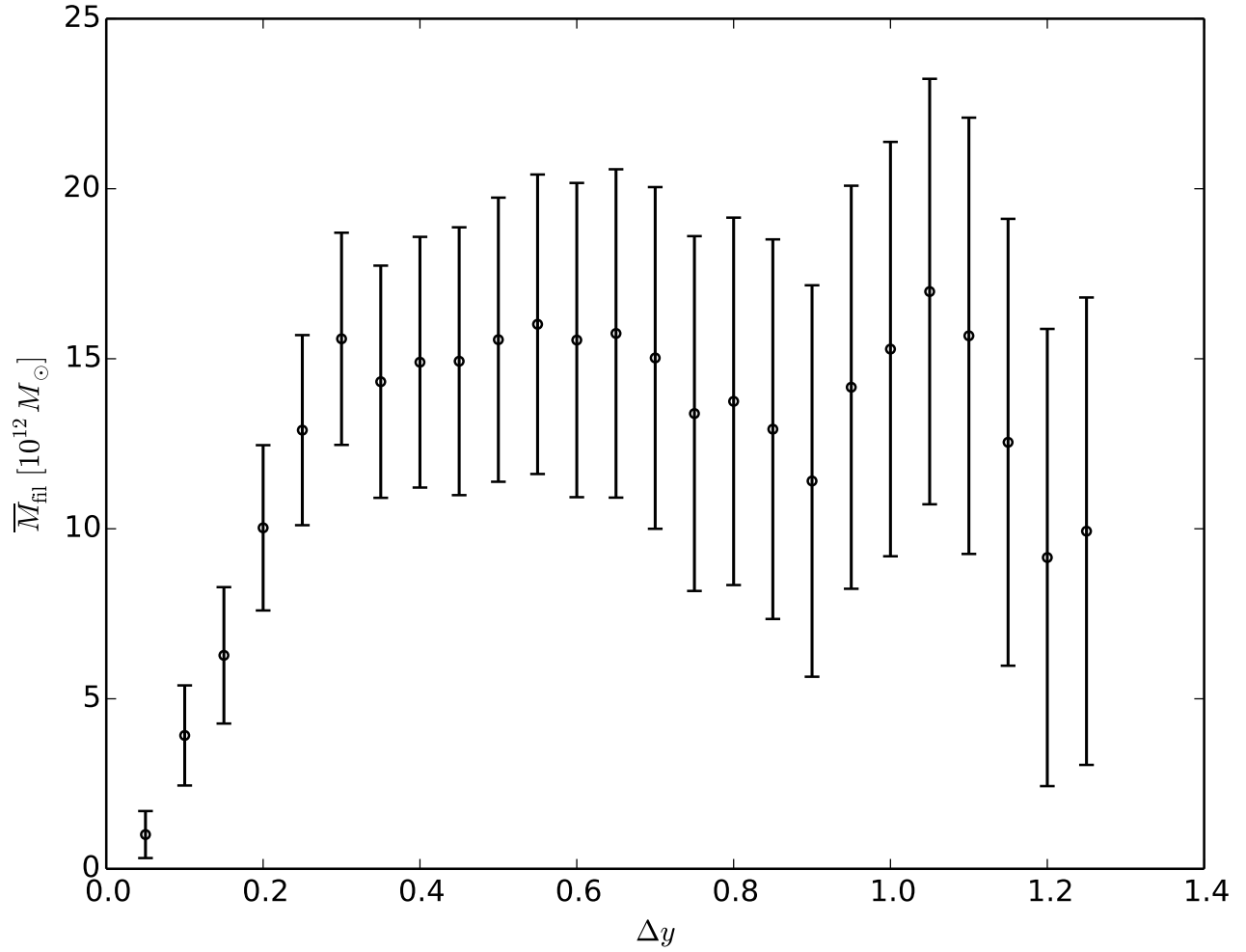
Figure 2.9: The average mass contained within the box defined by $\Delta x \times \Delta y$. The filament mass shows no sign of increasing beyond $\Delta y = 0.3$ (a physical width of $\sim 2.5h^{-1}\mathrm{Mpc}$). Hence we adopt this as the fiducial filament width.

Chapter 3

3-Point Correlation Function

Modelling the stacked filament accurately is a difficult task as there is no easy way to parameterize the non-linear structure with a firm theoretical basis. The proposed model here is based off the galaxy-galaxy-convergence (ggκ) 3-point correlation function (3PCF) derived from perturbation theory and developed in Clampitt et al. (2014). In §3.1 we re-derive the three point correlation function as done in Clampitt et al. (2014) with a slightly different notation.

3.1   Galaxy-Galaxy-κ Correlation Function

Here we are interested in the projected 3PCF among two dark matter halos at fixed locations $\vec{x}_1$ and $\vec{x}_2$, relative some matter at $\vec{x}_3$ which mathematically is just,

$$\zeta_{\mathrm{gg}\kappa}(\vec{x}_1, \vec{x}_2, \vec{x}_3) = \langle \delta_{\mathrm{g}}(\vec{x}_1)\delta_{\mathrm{g}}(\vec{x}_2)\kappa(\vec{x}_3)\rangle, \tag{3.1}$$

where δ_{g} is just the projected 3-dimensional galaxy overdensity which can easily be written in terms of the matter over density using some galaxy-matter bias parameter b,

$$\delta_{\mathrm{g}} = \int d\chi p(\chi)\delta_{\mathrm{g}}^{\mathrm{3D}}(\vec{x}) = \int d\chi b p(\chi)\delta_{\mathrm{m}}(\vec{x}). \tag{3.2}$$

The integral in (3.2) is over the line-of-sight separation and $p(\chi)$ is the probability distribution of either halo. κ is simply the integral over the matter overdensity along the line-of-sight weighted by $\Sigma_{\mathrm{crit}}^{-1}$ at a fixed source plane χ_{s},

$$\kappa = \int d\chi \Sigma_{\mathrm{crit}}^{-1}(\chi, \chi_{\mathrm{s}})\rho_{\mathrm{crit},0}\Omega_{\mathrm{m},0}\delta_{\mathrm{m}}(\vec{x}). \tag{3.3}$$

36

Combining (3.2) and (3.3), (3.1) becomes,

$$
\begin{aligned}
\zeta_{\mathrm{gg}\kappa}(\vec{x}_1, \vec{x}_2, \vec{x}_3) &= \int d\chi_1 d\chi_2 d\chi_3 p_1(\chi_1) p_2(\chi_2) \\
&\times \ \Sigma_{\mathrm{crit}}^{-1}(\chi_3, \chi_{\mathrm{s}}) \rho_{\mathrm{crit},0} \Omega_{\mathrm{m},0} b^2 \\
&\times \ \langle \delta_{\mathrm{m}}(\vec{x}_1) \delta_{\mathrm{m}}(\vec{x}_2) \delta_{\mathrm{m}}(\vec{x}_3) \rangle .
\end{aligned}
\tag{3.4}
$$

For the computing the integrals it makes more sense to re-write $\vec{x}_i$ as $\chi_i \vec{\theta}_i$, where the subscript corresponds to the subscripts in (3.4). Now the challenge is writing the third row of (3.4) in a way that it can be used. The fourier analogue to the 3PCF is the bispectrum, just as the fourier analogue of the two-point correlation function is the power spectrum, however the bispectrum is dependent on three k-space vectors instead of two,

$$
\begin{aligned}
\langle \delta_{\mathrm{m}}(\vec{x}_1) \delta_{\mathrm{m}}(\vec{x}_2) \delta_{\mathrm{m}}(\vec{x}_3) \rangle &= \int \frac{d^3 \vec{k}_1 d^3 \vec{k}_2 d^3 \vec{k}_3}{(2\pi)^6} B_{\mathrm{mmm}}(\vec{k}_1, \vec{k}_2, \vec{k}_3) \\
&\times \ \delta_{\mathrm{D}}^3(\vec{k}_1 + \vec{k}_2 + \vec{k}_3) \\
&\times \ \exp\left[i \left(\vec{x}_1 \cdot \vec{k}_1 + \vec{x}_2 \cdot \vec{k}_2 + \vec{x}_3 \cdot \vec{k}_3 \right) \right],
\end{aligned}
\tag{3.5}
$$

where δ_{D} is the dirac delta function. The bispectrum to be used is the perturbation theory bispectrum, which is the simplest. In principle one could use the full halo model bispectrum which contains information about the 1-halo (all matter particles in the same halo), the 2-halo (2 matter particles in one halo, and 1 particle in another), and the 3-halo (all matter particles in separate halos) terms, but for our purposes we only need the 3-halo contribution which is simply the perturbation theory bispectrum. The perturbation theory bispectrum is given by Bernardeau et al. (2002),

$$
\begin{aligned}
B(\vec{k}_1, \vec{k}_2, \vec{k}_3) &= \left[\frac{10}{7} + \left(\frac{k_1}{k_2} + \frac{k_2}{k_1} \right) \frac{\vec{k}_1 \cdot \vec{k}_2}{k_1 k_2} + \frac{4}{7} \frac{(\vec{k}_1 \cdot \vec{k}_2)^2}{k_1^2 k_2^2} \right] P_{\mathrm{m}}^{\mathrm{L}}(k_1) P_{\mathrm{m}}^{\mathrm{L}}(k_2) \\
&+ \ \text{permutations},
\end{aligned}
\tag{3.6}
$$

where $P_{\mathrm{m}}^{\mathrm{L}}(k)$ is the linear matter power spectrum (1.6).

To quantify the probability distributions in (3.4), we want to mimic the measurement as closely as possible. Since the spectroscopic data is taken from SDSS, the redshifts of the LRGs used is more or less known accurately, however there will always be some uncertainty in the true location of the cluster in redshift space due to various effects (*e.g.* peculiar velocities). To model these uncertainties we fix one LRG to be exactly at its

redshift, but let the other have some finite width relative to the other parameterized by a normal distribution,

$$
\begin{aligned}
p_1(\chi_1) &= \delta_{\mathrm{D}}(\chi_1 - \chi_{\mathrm{L}}) \\
p_2(\chi_2) &= \frac{1}{\sqrt{2\pi}\sigma_{\mathrm{LRG}}} \exp\left[-\frac{(\chi_2 - \chi_1)^2}{\sigma_{\mathrm{LRG}}^2}\right].
\end{aligned}
\tag{3.7}
$$

To further simplify the integral in (3.4) we use the approximation that $\chi_1 \approx \chi_2 \approx \chi_3$, which is just to say that all of the structures we are concerned with lie in the same plane. With the Dirac delta functions in (3.5) and (3.7), we can not only simplify (3.6), but also simplify the integrals over k-space. First we project the two k-space integrals into polar coordinates, which gives us an additional factor of $(2\pi)^2$ by using the identity

$$
\delta_{\mathrm{D}}(x - a) = \frac{1}{2\pi} \int_{-\infty}^{\infty} e^{i(x-a)t} dt.
\tag{3.8}
$$

Now the bispectrum (3.6) reduces to,

$$
\begin{aligned}
B(k_1, k_2, -k_{12}) = P_{\mathrm{m}}^{\mathrm{L}}(k_{12}) \quad \times \quad & \left\{ \left[\frac{10}{7} + \left(\frac{k_1}{k_{12}} + \frac{k_2}{k_{12}}\mu\right)\left(\frac{3}{7}\frac{k_1}{k_{12}} + \frac{k_{12}}{k_1} - \frac{4}{7}\frac{k_2}{k_{12}}\mu\right)\right] P_{\mathrm{m}}^{\mathrm{L}}(k_1) \right. \\
+ \quad & \left[\frac{10}{7} + \left(\frac{k_2}{k_{12}} + \frac{k_1}{k_{12}}\mu\right)\left(\frac{3}{7}\frac{k_2}{k_{12}} + \frac{k_{12}}{k_2} - \frac{4}{7}\frac{k_1}{k_{12}}\mu\right)\right] P_{\mathrm{m}}^{\mathrm{L}}(k_2) \right\} \\
+ \quad & \left[\frac{10}{7} + \mu\left(\frac{k_1}{k_2} + \frac{k_2}{k_1}\right) + \frac{4}{7}\mu^2\right] P_{\mathrm{m}}^{\mathrm{L}}(k_1) P_{\mathrm{m}}^{\mathrm{L}}(k_2)
\end{aligned}
\tag{3.9}
$$

where I have expanded all dot products in lieu of vector notation, used μ as the cosine of the angle between $\vec{k}_1$ and $\vec{k}_2$, and substituted $k_{12} = |\vec{k}_1 + \vec{k}_2|$. Now (3.4) simplifies to

$$
\begin{aligned}
\zeta_{\mathrm{gg}\kappa}(\vec{x}_1, \vec{x}_2, \vec{x}_3) &= \int d\chi_3 p_1(\chi_3) p_2(\chi_3) \Sigma_{\mathrm{crit}}^{-1}(\chi_3, \chi_{\mathrm{s}}) \rho_{\mathrm{crit},0} \Omega_{\mathrm{m},0} b^2 \\
&\times \int \frac{d^2\vec{k}_1 d^2\vec{k}_2}{(2\pi)^4} B(k_1, k_2, -k_{12}) \\
&\times \exp i\chi_3\left[\vec{k}_1 \cdot \left(\vec{\theta}_1 - \vec{\theta}_3\right) + \vec{k}_2 \cdot \left(\vec{\theta}_2 - \vec{\theta}_3\right)\right].
\end{aligned}
\tag{3.10}
$$

Because of the dirac delta function in (3.7) the first integral in (3.10) is trivial, leaving only the integrals in k-space. Since we want to know the value of the 3PCF at every possible $\vec{\theta}_3$ in the plane of the lenses, it makes sense to work in a coordinate system where $\vec{\theta}_3 = \vec{0}$. In this coordinate system, the distance to either $\vec{R}_1$ or $\vec{R}_2$ is just $R_i = \chi\theta_i$, where $\theta_i = |\vec{\theta}_i|$

38

and $R_i = |\vec{R}_i| = \chi \theta_i$.

To evaluate the integral over k-space, it is re-written in terms of the magnitudes, the angle between $\vec{k}_1$ and $\vec{k}_2$, and the angle between $\vec{k}_1$ and $\vec{R}_1$. In terms of these variables, the argument of the exponential in (3.10) becomes,

$$
\begin{aligned}
i\chi \left[\vec{k}_1 \cdot \vec{\theta}_1 + \vec{k}_2 \cdot \vec{\theta}_2 \right] &= i \left[k_1 R_1 \cos \psi + k_2 R_2 \cos(\psi + \phi - \lambda) \right] \\
&= i \left(\alpha \cos \psi - \beta \sin \psi \right),
\end{aligned} \tag{3.11}
$$

where I have used λ as the angle between $\vec{R}_1$ and $\vec{R}_2$ and ψ as the angle between $\vec{k}_1$ and $\vec{R}_1$, and the coefficients α and β are,

$$
\begin{aligned}
\alpha &\equiv R_1 k_1 + R_2 k_2 \cos(\phi - \lambda) \\
\beta &\equiv R_2 k_2 \sin(\phi - \lambda).
\end{aligned}
$$

Using this change of variables in (3.11), (3.10) simplifies to

$$
\begin{aligned}
\zeta_{gg\kappa}(\vec{x}_1, \vec{x}_2, \vec{x}_3) &= \frac{\Sigma_{\mathrm{crit}}^{-1}(\chi_{\mathrm{L}}, \chi_{\mathrm{s}})}{\sqrt{2\pi}\sigma_{\mathrm{LRG}}} \rho_{\mathrm{crit},0} \Omega_{\mathrm{m},0} b^2 \frac{1}{(2\pi)^4} \\
&\times \int_0^\infty dk_1 \int_0^\infty dk_2 \int_0^{2\pi} d\phi \, k_1 k_2 B(k_1, k_2, -k_{12}) \\
&\times \int_0^{2\pi} d\psi \exp\left[i \left(\alpha \cos \psi - \beta \sin \psi \right) \right].
\end{aligned} \tag{3.12}
$$

The last line of (3.12) integrates to the bessel function of the first kind,

$$
\int_0^{2\pi} d\psi \exp\left[i \left(\alpha \cos \psi - \beta \sin \psi \right) \right] = 2\pi \mathrm{J}_0(\sqrt{\alpha^2 + \beta^2}), \tag{3.13}
$$

provided that α and β are positive and real. This leaves

$$
\begin{aligned}
\zeta_{gg\kappa}(\vec{x}_1, \vec{x}_2, \vec{x}_3) &= \frac{\Sigma_{\mathrm{crit}}^{-1}(\chi_{\mathrm{L}}, \chi_{\mathrm{s}})}{\sqrt{2\pi}\sigma_{\mathrm{LRG}}} \rho_{\mathrm{crit},0} \Omega_{\mathrm{m},0} b^2 \frac{1}{(2\pi)^3} \\
&\times \int_0^\infty dk_1 \int_0^\infty dk_2 \int_0^{2\pi} d\phi \, k_1 k_2 B(k_1, k_2, -k_{12}) \\
&\times \mathrm{J}_0(\sqrt{\alpha^2 + \beta^2}),
\end{aligned} \tag{3.14}
$$

39

which can now be evaluated numerically for a given separation bin as described in §2.1.2. Note that R_1 and R_2 are in comoving coordinates, however the separation bins are grouped by physical separation. Before numerically integrating (3.14), the separation bin must be converted to comoving coordinates.

The three-point convergence map generated for the separation bin $6h^{-1}\text{Mpc} \leq R_\text{sep} < 10h^{-1}\text{Mpc}$ is show in Figure 3.1. Here we use a linear bias, b, of 2 (More et al., 2015b; Tojeiro et al., 2014) and, following Clampitt et al. (2014), estimate that the effect of peculiar velocities gives $\sigma_\text{LRG} \sim 8h^{-1}\text{Mpc}$. Here we are careful to ensure that the resulting convergence map is in physical units; the integral in (3.14) is done over comoving coordinates, which introduces an additional factor of $(1 + z_l)^{-2}$. The Σ_crit was measured from the data according to (2.12).

3.2   3PCF Shear Map

Since the data is measured in shear space, in some cases it may be more natural to work in the three-point correlation shear space rather than the convergence space. Just as in §2.2.3, where the shear map was converted into a convergence map, the inverse can also be done by solving (1.18).

The resulting shear map, shown in Figure 3.2, has quite a few distinct features. First, the largest shear is located at the midpoint of the cluster locations. In the region we expect to have a filament, there's negative γ_1 shear component, and very little γ_2. As you move away from the filament in the $\pm y$ direction, the γ_1 component transitions into a positive value. In the regions around the clusters ($x = \pm 0.5$), there's appears to be a slight amount tangential shear about the respective halos, however this is more of a qualitative appearance.

3.3   Results

In this section, we present the results from Chapter 2 in the context of the three-point correlation function, applying the methods of subtracting the LRG signal from §2.3 to both the data and model three-point correlation function.
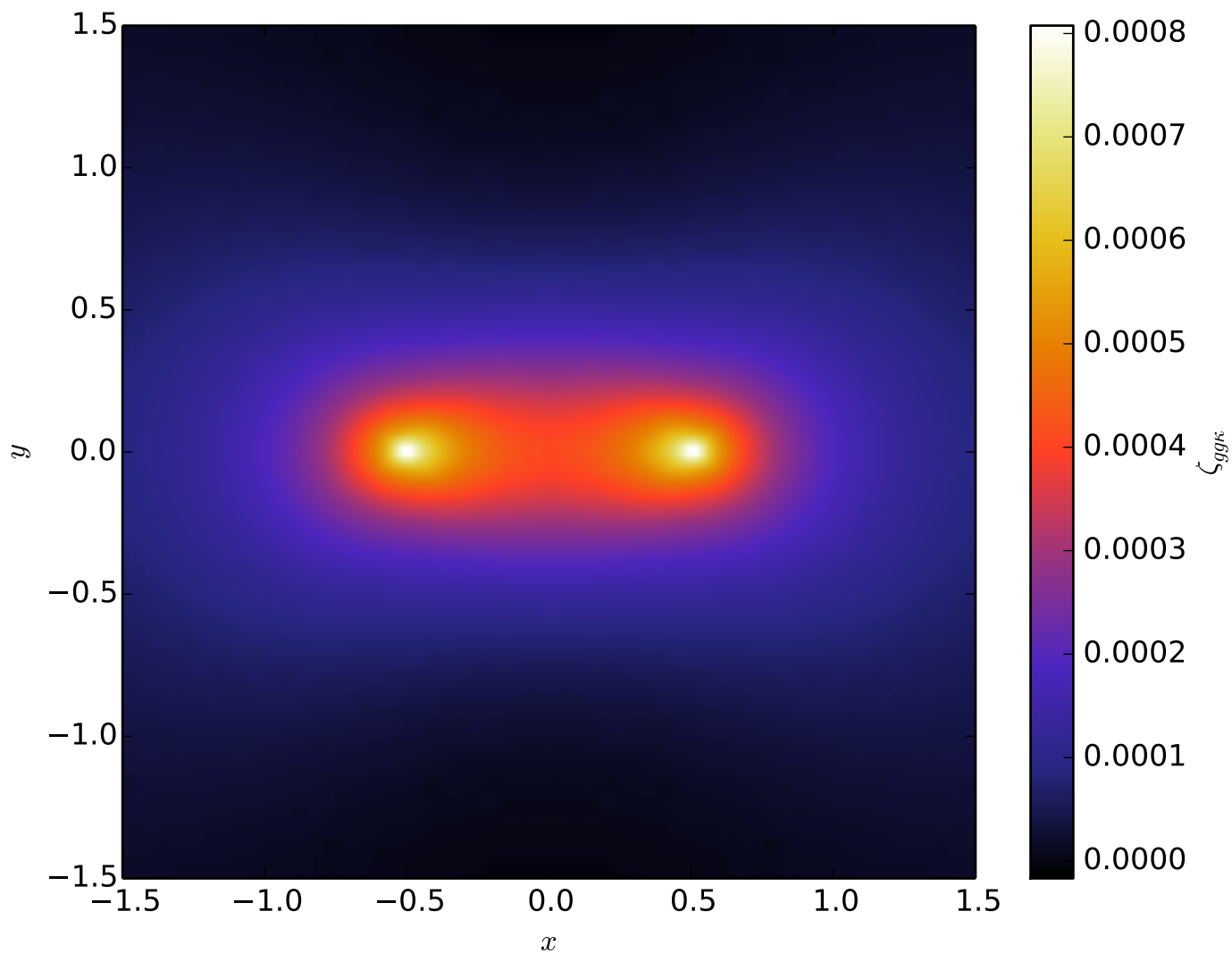
Figure 3.1: The three-point galaxy-galaxy-convergence calculated by numerically integrating (3.14) for the separation bin $6h^{-1}\mathrm{Mpc} < R < 10h^{-1}\mathrm{Mpc}$. This is plotted in the standardized coordinate system defined in §2.2.1.
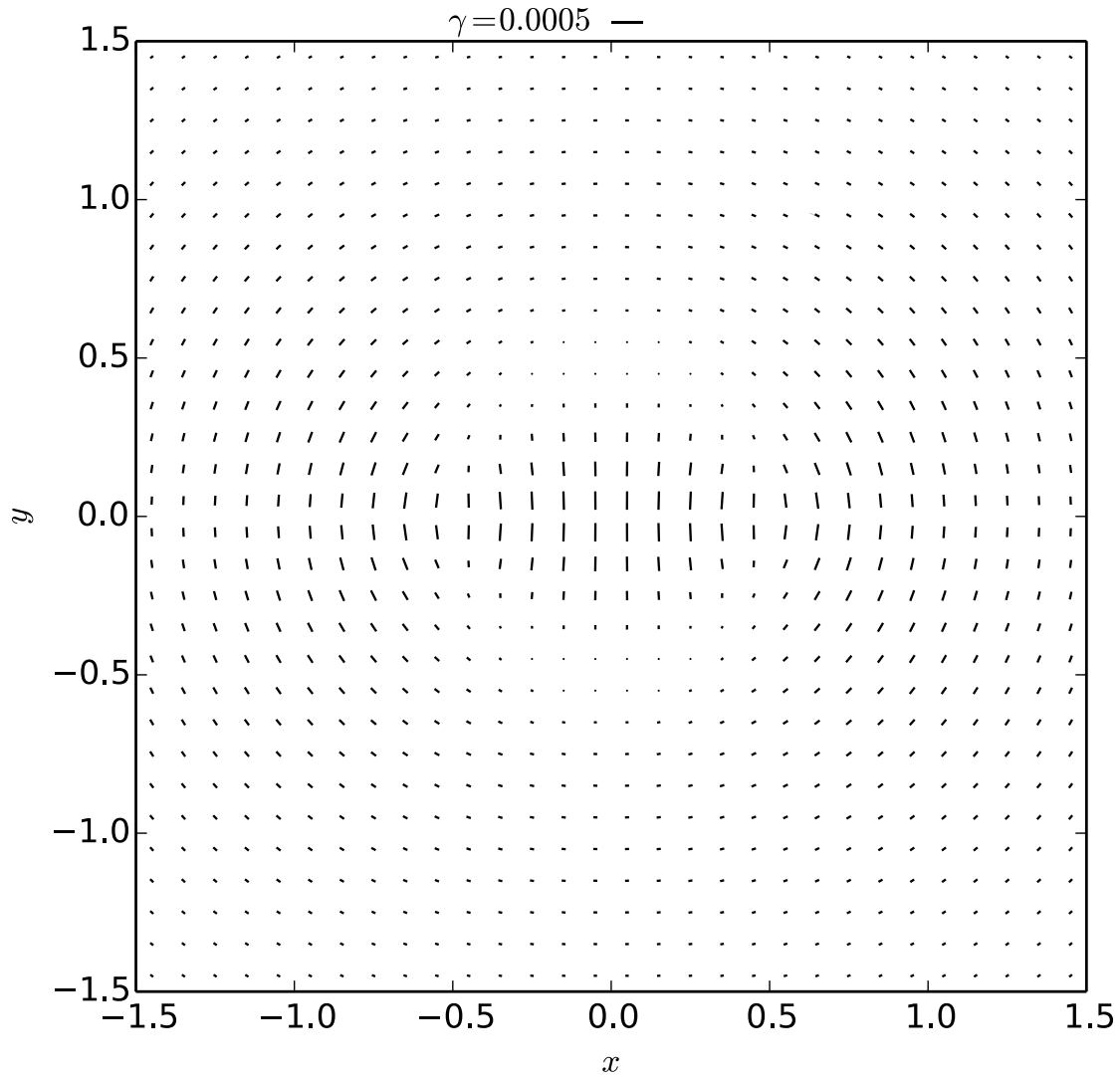
Figure 3.2: The shear map corresponding to the three-point galaxy-galaxy-convergence in Figure 3.1. This was obtained by performing a Kaiser & Squires inversion (§1.2.2) on the convergence map in Figure 3.1. This is also plotted in the standardized coordinate system defined in §2.2.1.

3.3.1 Non-Physical Pair Subtraction

As mentioned in 2.3.1 the method of non-physical pair subtraction is easier to interpret in convergence space so it makes most sense to work exclusively in convergence space. Just as in §2.4, we start by subtracting the signal from stacking non-physical pairs from the signal of physical pairs, giving the residual convergence map in Figure 2.7. Since we do not expect this subtraction to affect the resulting filament signal, nothing must be done to the model three-point correlation function. Again, we restrict the range of x to be outside $2x_{200}$ of either LRG to avoid any LRG contribution, however instead of taking the average over a box placed over the filament, we bin in vertical strips along the x-axis for a particular Δy.

As was discussed in §2.4, the filament signal flattened out at a fiducial width of $\Delta y = 0.3$ so this is the value we use for comparison. Figure 3.3 shows convergence data binned along x-axis as well as the the three-point correlation function, averaged over the fiducial width. Plotted as well is the total averaged convergence within the filament box. At a glance, it appears the three-point function fits the data well, however the model lies slightly above the best fitting value. Performing a least squares fit shows that the model is over estimated by a factor of ~ 1.6.

3.3.2 Outside Region Subtraction

In §2.4 we found that the width of the filament region that maximizes the signal to noise was $\Delta y = 0.3$, so here we use the same fiducial width. Applying the outside region subtraction to the three point function and the data, we see that the model is under estimated compared to the data. Figure 3.4 shows the three-point correlation function plotted over the data after the outside regions have been subtracted from the inner regions after re-scaling the model. Performing a least squares fit to the overall scale of the model shows that the model is smaller than the data by a factor of ~ 10.

3.3.3 Discussion

The two methods of isolating the filament signal above are expected to produce a similar signal, and in principle should give the same results in comparison to the three-point correlation function, but this is not the case. One may be concerned with systematics in the measurement of the filament signal, in which case the method of non-physical pair subtraction is a much better method for model comparisons. Any systematics present
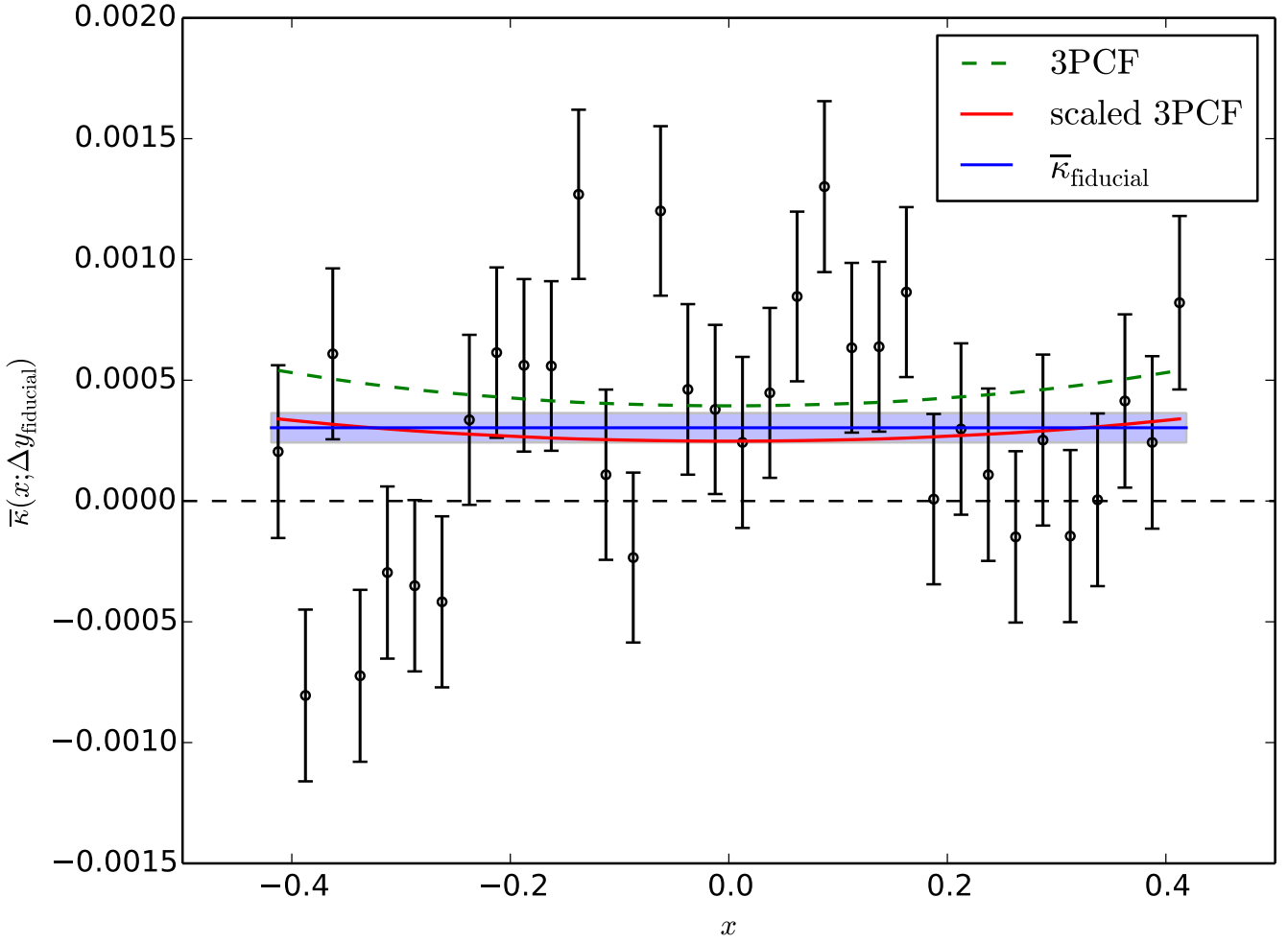
Figure 3.3: The resulting convergence profile along the x-axis for the method of non-physical pair subtraction. This is done for the fiducial Δy calculated in §2.4, with the average convergence for that particular box plotted in blue. The model three-point correlation function is plotted in green and the model scaled down by a factor of 0.6 is plotted in red. For comparison the mean convergence within the fiducial width is also shown in blue.
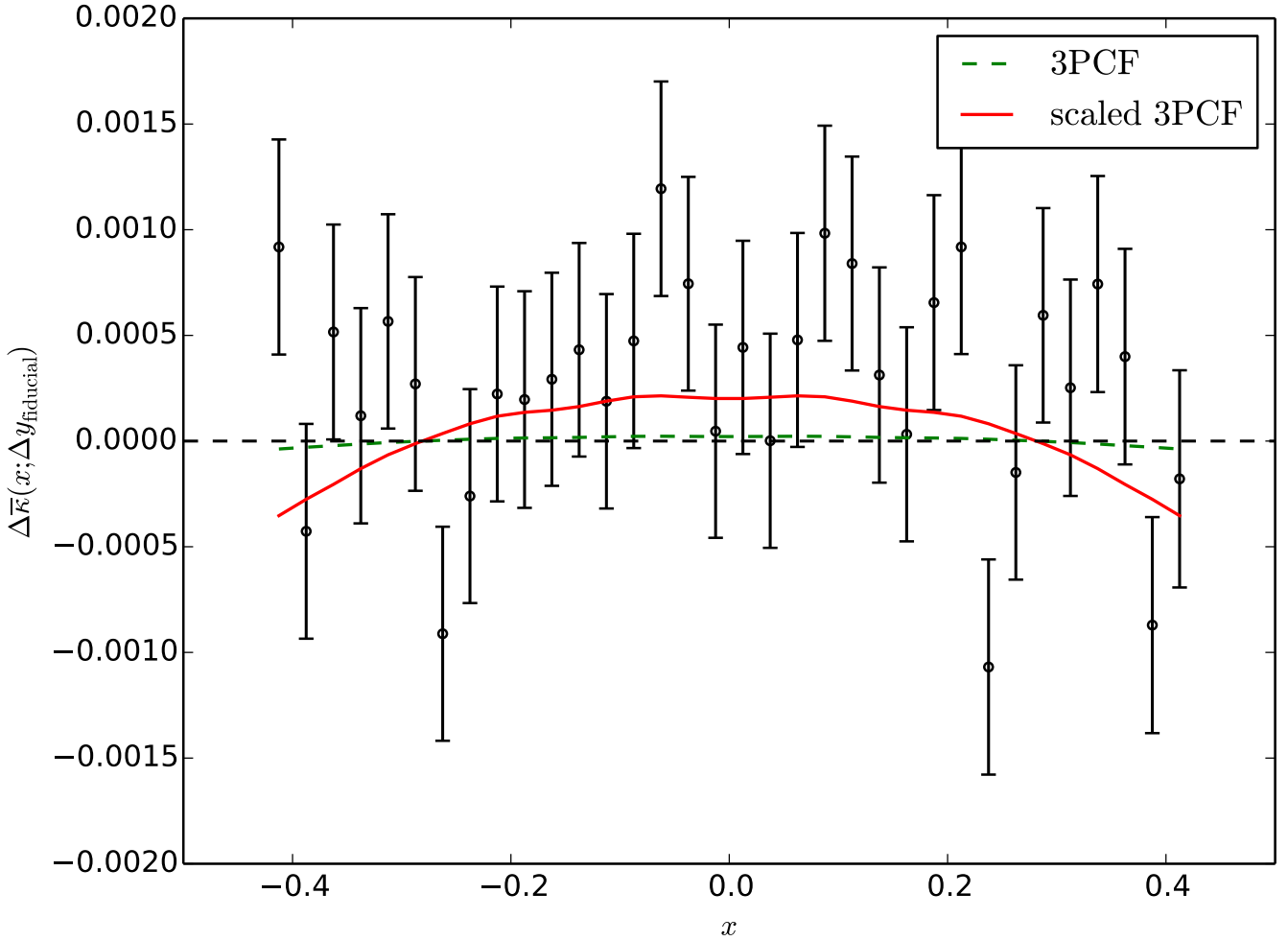
Figure 3.4: The resulting convergence profile along the x-axis for the method of outside region subtraction. This is done for the fiducial Δy calculated in §2.4. The model three-point correlation function is plotted in green and the model scaled up by ~ 10 is plotted in red.

in the weak lensing signal of the physical pairs would also be present in the non-physical pairs, in which case we'd expect these systematics to be nulled out in the direct subtraction.

When performing the outside region subtraction the regions just beyond either LRG may have contributions from the opposite LRG. This would introduce additional convergence in the three-point function that extends from either LRG halo to the outside regions of the other. This leads to an over subtraction in the filament region. This required scaling when using the outside region subtraction is still not well understood and requires more investigation.

The required scaling of the model in the case of non-physical pair subtraction is relatively small, being on the order of uncertainty in the data (roughly 20%). The simplest explanation for the scaling would be that contamination to the LRG sample, for example a misclassification of a galaxy, could introduce noise to the weak lensing signal effectively lowering the filament convergence. Alternatively a potential source for this overestimate of the model is *under*estimate of the effect from the LRG peculiar velocities. If this uncertainty in the relative LRG positions in redshift space, σ_{LRG},was increased to $\sim 13h^{-1}\mathrm{Mpc}$, there would be no need to scale the model.

In the three-point correlation function model we follow Clampitt et al. (2014), parameterizing the line-of-sight distribution of a second LRG by a gaussian distribution describing the relative motions of the LRG pair. In hindsight, although it may be a good approximation, this model can be improved by using a more physically motivated distribution, using two-point statistics. We know that the probability of finding a neighbouring galaxy at distance r from the first is (Peebles, 1980)

$$dP \propto [1 + \xi(r)]dV, \qquad (3.15)$$

where ξ is the two point correlation function defined in (1.7) and dV is the volume element in which the second galaxy would be found. The radial distance, r, can be broken up into two components, one line-of-sight and the other the separation. Marginalizing over the separation, one could use this probability density combined with the effect of relative motions to improve (3.7). The effect of using this approach of the two-point correlation function is to be further investigated in the future.

In this work, particularly when isolating the filament using the method of non-physical pair subtraction, we find a relatively good agreement with the data. Clampitt et al. (2014) investigated the the same model of stacked filaments with a different method of removing the circularly symmetric components of the LRG signal. They found large discrepancy

between the three-point correlation function model and the data, finding the model prediction to be ~ 10 times larger than the data.

The sample of LRGs used in Clampitt et al. (2014) were also selected from SDSS, similar to the LRGs used in this study. However they find that the stacked filament is more massive than the halos that connect to it. This not seen in other reports of individual filaments connecting even more massive clusters of galaxies. Dietrich et al. (2012) found that for two galaxy clusters of mass $\sim 2 \times 10^{14} M_\odot$ the filament had mass of $6.5 \times 10^{13} M_\odot$, and Higuchi et al. (2015) found that for clusters of mass larger masses (up to $10^{15} M_\odot$) the filament remained smaller at $3.2 \times 10^{14} M_\odot$. This holds true here, with the mass of a typical LRG halo being $\sim 10^{13} M_\odot$ giving a filament of similar mass at $1.6 \times 10^{13} M_\odot$.

Chapter 4

Conclusions

The formation of a filamentary structure that intersects at high density collapsed regions of the universe is a prediction from simulations that has only recently become detectable observationally. In this work we have presented the methodology required to combine the weak lensing signal from many filaments, and successfully detected a stacked filamentary structure between SDSS BOSS LRGs with the CFHTLenS data set. The filament detection is significant at the 5σ level, with a mass of $(1.6 \pm 0.3) \times 10^{13} M_{\odot}$ for a box of fiducial physical dimensions, $6.8 \times 2.4 h^{-1}\mathrm{Mpc}$. We have presented two methods of isolating the filament signal from the LRG signal, the method of non-physical pairs being a more promising method. The three-point correlation function is used as a model for the stacked filament, derived from the perturbation theory bispectrum. We have shown that the three-point correlation function fits reasonably to the data, only needing to be rescaled by a factor of 0.63 ± 0.20 after isolating the filament signal from the LRGs. Using the method of outside region subtraction the model was found to be factor of 9.4 ± 5.4 smaller than the data which is not well understood.

The notion of stacking filaments provides a statistical interpretation of an ensemble of filaments, whereas previous studies have investigated individual filaments (Dietrich et al., 2012; Higuchi et al., 2015). Clampitt et al. (2014) present a similar study of stacked filaments in SDSS, claiming a 10σ detection. They modelled the stacked filament using the three-point correlation function, but found the model was a factor 10 larger than the data. Here, we find that only a small amount of re-scaling is required, at least when the LRG signal is removed by non-physical pair subtraction. The origin of the required scaling of the model is unclear. There are various reasons one might need to scale the model, ranging from a contaminated sample of LRGs, to a poorly understood method of isolating the fila-

ment signal, even poor modelling of certain phenomena. We suggest that the model can be improved by combining line-of-sight distribution of LRGs with two-point galaxy clustering statistics, however it is unclear how this will change the model and will be investigated in upcoming publication. An alternative to comparing with the three-point correlation function is to directly compare with the stacked density profiles of filaments in N-body simulations. This will give insight to how well the three-point correlation function models the filaments, and improve our understanding of the required scaling.

The goal of this study was to detect filaments using weak lensing, but more importantly serve as the foundation for future filament studies. We have developed a method of stacking filaments that can be applied to any weak lensing experiments provided one has obtained redshifts for groups and clusters of galaxies through spectroscopy. Although CFHTLenS is the current best weak lensing dataset, upcoming surveys will soon greatly improve our ability to do weak lensing studies, with ongoing experiments such as DES collecting data hundreds of millions of galaxies, to the same depth as CFHTLenS (The Dark Energy Survey Collaboration, 2005). Presently there is little spectroscopy in the DES footprint. There is also a proposal to survey the equivalent coverage of SDSS to nearly the same depth of CFHTLenS (personal communication, Hudson 2015). As well as new ground based experiments, there are planned space-based experiments that will do much better, such as Euclid or WFIRST, with potential to measure the shapes and photometry of billions of galaxies, not susceptible to limitations of ground based experiments (Mellier, 2012; Spergel et al., 2015). These space based experiments will be equipped with on board spectrographs, allowing for the estimation of deeper spectroscopic redshifts along with the improved photometry.

APPENDICES

Appendix A

Alternative Methods of Isolating Filament Signal

Here we present two alternative methods for isolating the filament signal from the circularly symmetric signal around the LRGs. These two methods have not been fully investigated, and hence they are only outlined here, but will be applied to the data in a future publication.

A.1   90 Degree "Nulling"

The method of 90 degree nulling was introduced in Clampitt et al. (2014), and is a relatively straightforward way to remove the circularly symmetric components around around a single LRG. It relies on the fact that tangential shears at points 90° to one another (on a circle of constant radius) will have equal, but opposite sign, γ_1 and γ_2 components. Therefore the average of the shear at these points will cancel leaving 0 shear contribution. As a schematic, take an LRG in the standardized coordinate system (see 2.2.1) at $(x_L, y_L) = (-0.5, 0)$. Imagine a point, p1, that lies on an imaginary circle at some radius away from the LRG centre. Now imagine another point, p2, that lies on the same circle, but at 90° to p1, as in Figure A.1. For a spherically symmetric lens, these two shears will average to 0.

In the case of the LRG pair things are more complicated, as one can imagine the shear signal as a superposition of the signal from the two individually. Naturally this will distort

the purely tangential nature of the shears about their respective LRG so for a given point the signal contribution from both LRGs must be removed. Now imagine *two* LRGs in the standardized coordinate system at $(x_L, y_L) = (-0.5, 0)$ and $(x_R, y_R) = (0.5, 0)$, placing the same points p1 and p2 on an imaginary circle relative to the left LRG.

The points p1 and p2 no longer only lie on the circle relative to the left LRG, but on two other circles relative to the right LRG (see Figure A.2). The corresponding points that lie 90° to p1 (p3) and 90° to p2 (p4) on these new circles contains the shear contribution at p1 and p2 from the right LRG. In the case that both LRGs are spherically symmetric lenses, the shear at these four points will average to 0. One can also check that the points p3 and p4 do not introduce any additional contributions to the shear from the left cluster as they will also lie 90° to each other relative to the left cluster on their own imaginary circle.

With this method, depending on how the data is binned, the symmetry in γ_2 can be exploited as a systematic test, similar to the cross shear in galaxy-galaxy lensing. Since the nulling at each point is actually an average over 4 separate points, if the binning is done in vertical bins at a particular x, the bins will actually form a pattern of intersecting vertical and horizontal bins, where p1 and p3 become vertical bins, and p2 and p4 become horizontal bins. Each bin will have γ_1 components, but the γ_2 components are expected to cancel due to the symmetry of the filament signal. This symmetry of γ_2 gives a systematic test analogous to the cross shear in galaxy-galaxy lensing.

A.2 Mean Tangential Shear Subtraction

Rather than using a clever nulling scheme, one might be inclined to simply calculate the tangential shear about the individual cluster centres as a function of radius, and subtract it from the data. Unfortunately, using this approach will over subtract in the region of the filament. To visualize this, consider the situation in which there is no filament and, for simplicity, the two clusters have equal mass. Imagine two circles of equal radius, one centred on the left cluster and the other on the right cluster, that just touch at the centre axis $(0, 0)$. The tangential shear at these two points will sum, and that point will contribute twice the value it would had the clusters been isolated. Now if the tangential shear was calculated about the two clusters, that particular point would be in effect counted twice, giving 4 times the tangential shear.
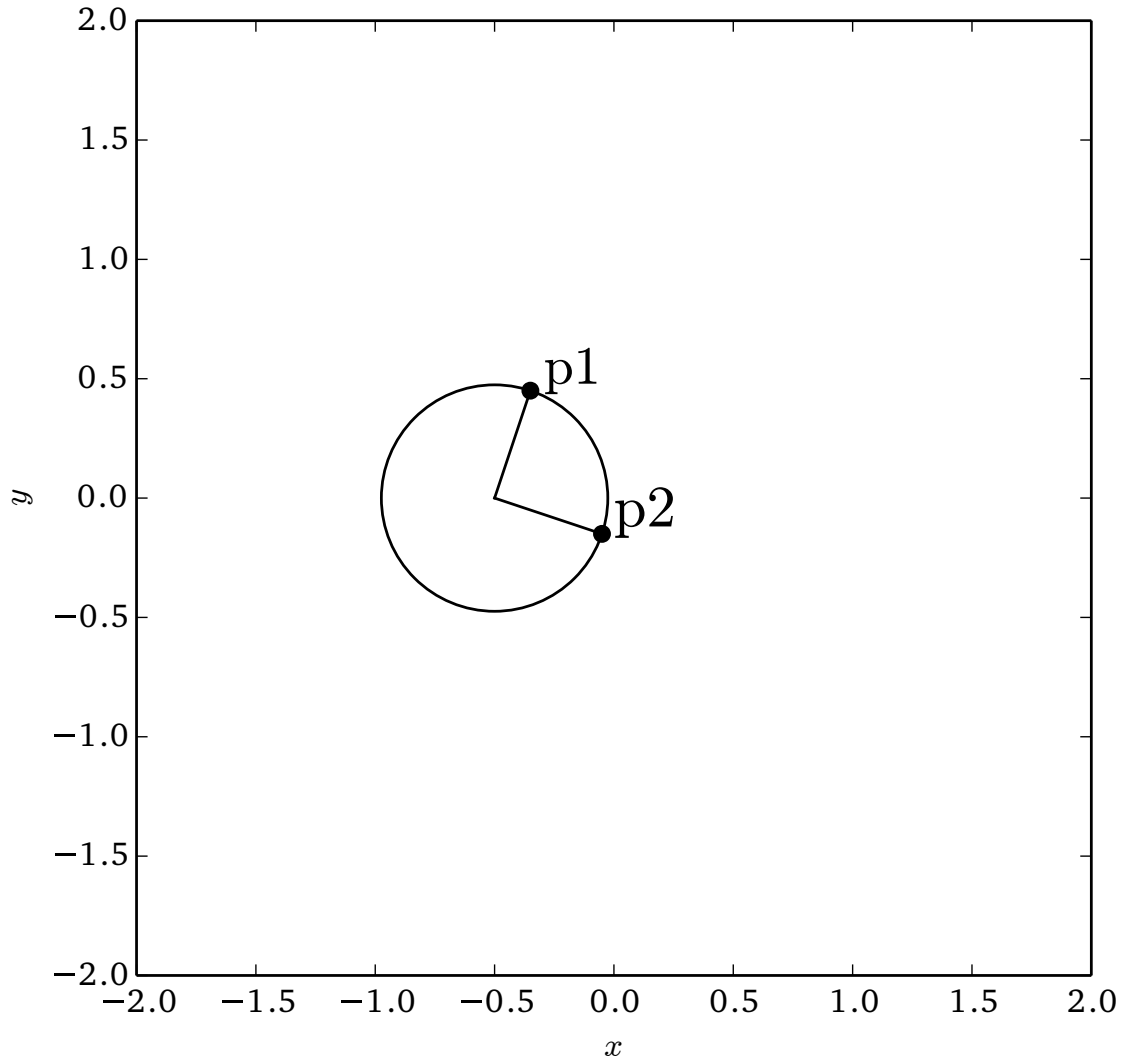
Figure A.1: This is a schematic for how the 90 degree nulling removes the circularly symmetric shear at p1, by adding in p2. For a spherically symmetric lens centred at $x = -0.5$, the shear components at p2 will be equal and opposite to p2.
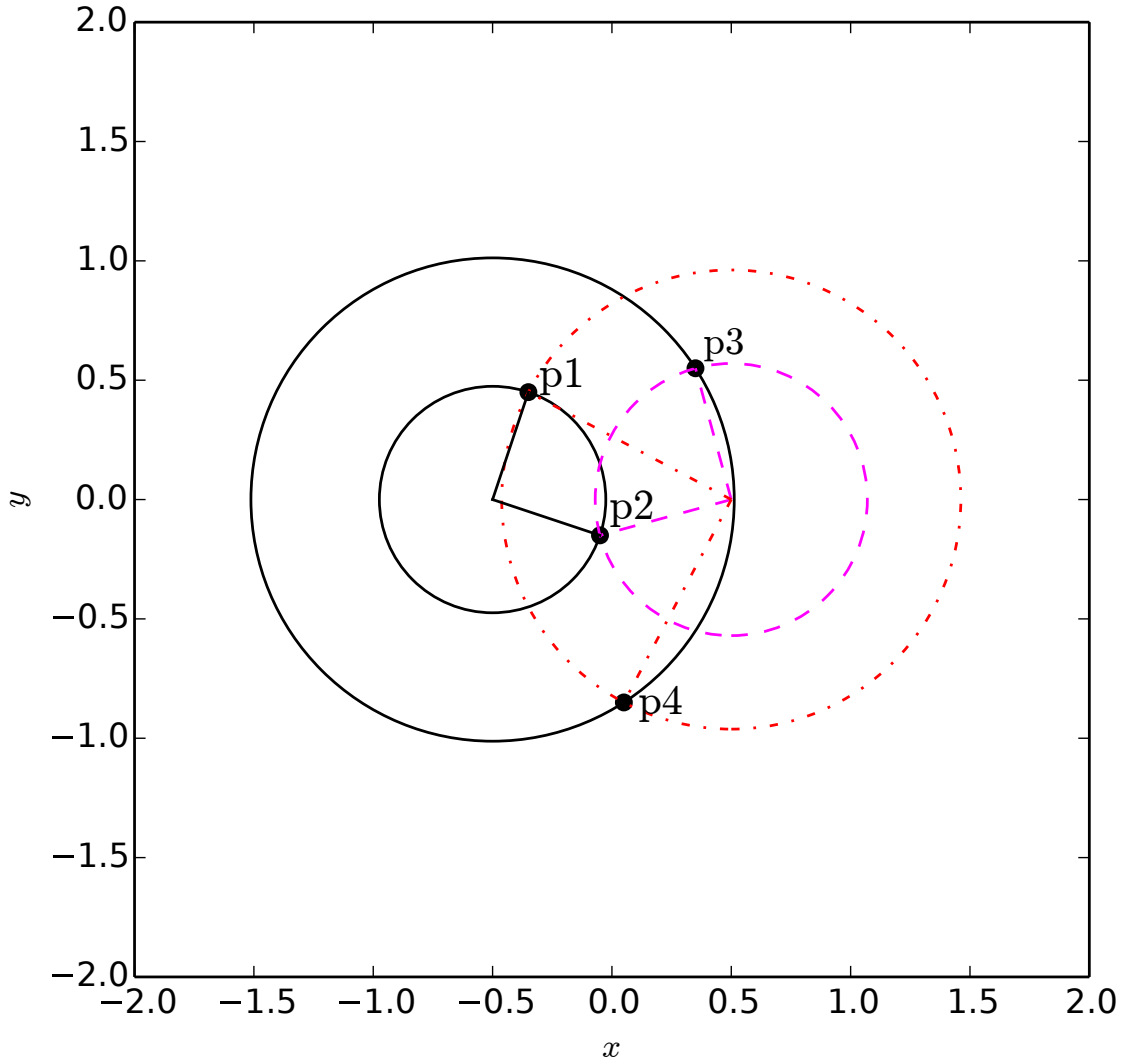
Figure A.2: This is a schematic for how the 90 degree nulling removes the circularly symmetric shear at p1, by adding in p2, p3, and p4. For two spherically symmetric lens' centred at $x = \pm 0.5$, the shear components can be thought of as a superposition of both LRG signals. As a result p1 will have contributions from the right LRG, which can be removed by averaging over p2, p3, and p4.

When calculating the mean tangential shear for a particular radial bin, the value of shears is taking from the entire annulus around it. As a result the point that gives 4 times the tangential shear will be averaged with many other points, of which may have negligible effect from the adjacent cluster. The net effect of the of this overlap is unclear. As in the the 90 degree subtraction, this method will also remove some of the filament signal, as it is possible the filament shear will have some tangential component about either LRG.

In the standard coordinate system used, the tangential shear about a given cluster centre can be calculated from,

$$\gamma_{\mathrm{T}}(R) = - \left[\gamma_1(R) \cos\left(2\tau\right) + \gamma_2(R) \sin\left(2\tau\right) \right], \tag{A.1}$$

where τ is the angle bin makes relative to the individual cluster. The tangential shear can be converted back into an $\gamma_{1;\mathrm{T}}$ and $\gamma_{2;\mathrm{T}}$ and subtracted from the data.

References

Benítez, N. Bayesian Photometric Redshift Estimation. *ApJ*, 536:571–583, June 2000. doi: 10.1086/308947.

Bernardeau, F., Colombi, S., Gaztañaga, E. et al. Large-scale structure of the Universe and cosmological perturbation theory. *Phys. Rep.*, 367:1–248, September 2002. doi: 10.1016/S0370-1573(02)00135-7.

Bond, J.R., Kofman, L. and Pogosyan, D. How filaments of galaxies are woven into the cosmic web. *Nature*, 380:603–606, April 1996. doi: 10.1038/380603a0.

Cautun, M., van de Weygaert, R., Jones, B.J.T. et al. Evolution of the cosmic web. *MNRAS*, 441:2923–2973, July 2014. doi: 10.1093/mnras/stu768.

Clampitt, J., Jain, B. and Takada, M. Detection of Stacked Filament Lensing Between SDSS Luminous Red Galaxies. *ArXiv e-prints*, February 2014.

Colberg, J.M., Krughoff, K.S. and Connolly, A.J. Intercluster filaments in a ΛCDM Universe. *MNRAS*, 359:272–282, May 2005. doi: 10.1111/j.1365-2966.2005.08897.x.

Connolly, A.J., Csabai, I., Szalay, A.S. et al. Slicing Through Multicolor Space: Galaxy Redshifts from Broadband Photometry. *AJ*, 110:2655, December 1995. doi: 10.1086/117720.

Dawson, K.S., Schlegel, D.J., Ahn, C.P. et al. The Baryon Oscillation Spectroscopic Survey of SDSS-III. *AJ*, 145:10, January 2013. doi: 10.1088/0004-6256/145/1/10.

Dietrich, J.P., Werner, N., Clowe, D. et al. A filament of dark matter between two clusters of galaxies. *Nature*, 487:202–204, July 2012. doi: 10.1038/nature11224.

Dolag, K., Borgani, S., Schindler, S. et al. Simulation Techniques for Cosmological Simulations. *Space Sci. Rev.*, 134:229–268, February 2008. doi: 10.1007/s11214-008-9316-5.

Erben, T., Hildebrandt, H., Miller, L. et al. CFHTLenS: the Canada-France-Hawaii Telescope Lensing Survey - imaging data and catalogue products. *MNRAS*, 433:2545–2563, August 2013. doi: 10.1093/mnras/stt928.

Goroff, M.H., Grinstein, B., Rey, S.J. et al. Coupling of modes of cosmological mass density fluctuations. *ApJ*, 311:6–14, December 1986. doi: 10.1086/164749.

Heymans, C., Van Waerbeke, L., Miller, L. et al. CFHTLenS: the Canada-France-Hawaii Telescope Lensing Survey. *MNRAS*, 427:146–166, November 2012. doi: 10.1111/j.1365-2966.2012.21952.x.

Higuchi, Y., Oguri, M., Tanaka, M. et al. Detection of a filament connected to CL0016 with weak gravitational lensing. *ArXiv e-prints*, March 2015.

Hildebrandt, H., Erben, T., Kuijken, K. et al. CFHTLenS: improving the quality of photometric redshifts with precision photometry. *MNRAS*, 421:2355–2367, April 2012. doi: 10.1111/j.1365-2966.2012.20468.x.

Hirata, C.M., Mandelbaum, R., Seljak, U. et al. Galaxy-galaxy weak lensing in the Sloan Digital Sky Survey: intrinsic alignments and shear calibration errors. *MNRAS*, 353: 529–549, September 2004. doi: 10.1111/j.1365-2966.2004.08090.x.

Hoshino, H., Leauthaud, A., Lackner, C. et al. Luminous red galaxies in clusters: central occupation, spatial distributions and miscentring. *MNRAS*, 452:998–1013, September 2015. doi: 10.1093/mnras/stv1271.

Hudson, M.J., Gillis, B.R., Coupon, J. et al. CFHTLenS: co-evolution of galaxies and their dark matter haloes. *MNRAS*, 447:298–314, February 2015. doi: 10.1093/mnras/stu2367.

Jain, B. and Bertschinger, E. Second-order power spectrum and nonlinear evolution at high redshift. *ApJ*, 431:495–505, August 1994. doi: 10.1086/174502.

Kaiser, N. and Squires, G. Mapping the dark matter with weak gravitational lensing. *ApJ*, 404:441–450, February 1993. doi: 10.1086/172297.

Kaiser, N., Squires, G. and Broadhurst, T. A Method for Weak Lensing Observations. *ApJ*, 449:460, August 1995. doi: 10.1086/176071.

Mandelbaum, R. Instrumental systematics and weak gravitational lensing. *Journal of Instrumentation*, 10:C05017, May 2015. doi: 10.1088/1748-0221/10/05/C05017.

Mandelbaum, R., Hirata, C.M., Seljak, U. et al. Systematic errors in weak lensing: application to SDSS galaxy-galaxy weak lensing. *MNRAS*, 361:1287–1322, August 2005. doi: 10.1111/j.1365-2966.2005.09282.x.

Mellier, Y. Euclid: Mapping the Geometry of the Dark Universe. In *Science from the Next Generation Imaging and Spectroscopic Surveys*, page 3, October 2012.

Miller, L., Heymans, C., Kitching, T.D. et al. Bayesian galaxy shape measurement for weak lensing surveys - III. Application to the Canada-France-Hawaii Telescope Lensing Survey. *MNRAS*, 429:2858–2880, March 2013. doi: 10.1093/mnras/sts454.

More, S., Diemer, B. and Kravtsov, A.V. The Splashback Radius as a Physical Halo Boundary and the Growth of Halo Mass. *ApJ*, 810:36, September 2015a. doi: 10.1088/0004-637X/810/1/36.

More, S., Miyatake, H., Mandelbaum, R. et al. The Weak Lensing Signal and the Clustering of BOSS Galaxies. II. Astrophysical and Cosmological Constraints. *ApJ*, 806:2, June 2015b. doi: 10.1088/0004-637X/806/1/2.

Navarro, J.F., Frenk, C.S. and White, S.D.M. A Universal Density Profile from Hierarchical Clustering. *ApJ*, 490:493–508, December 1997.

Padmanabhan, T. *Structure Formation in the Universe.* May 1993.

Peebles, P.J.E. *The large-scale structure of the universe.* 1980.

Planck Collaboration, Ade, P.A.R., Aghanim, N. et al. Planck 2015 results. XIII. Cosmological parameters. *ArXiv e-prints*, February 2015.

Schaye, J., Crain, R.A., Bower, R.G. et al. The EAGLE project: simulating the evolution and assembly of galaxies and their environments. *MNRAS*, 446:521–554, January 2015. doi: 10.1093/mnras/stu2058.

Schneider, P. Part 1: Introduction to gravitational lensing and cosmology. In Meylan, G., Jetzer, P., North, P. et al, editors, *Saas-Fee Advanced Course 33: Gravitational Lensing: Strong, Weak and Micro*, pages 1–89, 2006.

Simon, P., Erben, T., Schneider, P. et al. CFHTLenS: higher order galaxy-mass correlations probed by galaxy-galaxy-galaxy lensing. *MNRAS*, 430:2476–2498, April 2013. doi: 10.1093/mnras/stt069.

Spergel, D., Gehrels, N., Baltay, C. et al. Wide-Field InfrarRed Survey Telescope-Astrophysics Focused Telescope Assets WFIRST-AFTA 2015 Report. *ArXiv e-prints*, March 2015.

Takada, M. and Jain, B. The three-point correlation function in cosmology. *MNRAS*, 340: 580–608, April 2003. doi: 10.1046/j.1365-8711.2003.06321.x.

The Dark Energy Survey Collaboration. The Dark Energy Survey. *ArXiv Astrophysics e-prints*, October 2005.

Tojeiro, R., Ross, A.J., Burden, A. et al. The clustering of galaxies in the SDSS-III Baryon Oscillation Spectroscopic Survey: galaxy clustering measurements in the low-redshift sample of Data Release 11. *MNRAS*, 440:2222–2237, May 2014. doi: 10.1093/mnras/stu371.

Weygaert, R.V.D. and Bond, J.R. Clusters and the Theory of the Cosmic Web. In Plionis, M., Hughes, D. and López-Cruz, O., editors, *A Pan-Chromatic View of Clusters of Galaxies and the Large-Scale Structure*, volume 740 of *Lecture Notes in Physics, Berlin Springer Verlag*, page 335, 2008. doi: 10.1007/978-1-4020-6941-3_10.

Zel'dovich, Y.B. Gravitational instability: An approximate theory for large density perturbations. *A&A*, 5:84–89, March 1970.

Zwicky, F. Die Rotverschiebung von extragalaktischen Nebeln. *Helvetica Physica Acta*, 6: 110–127, 1933.